Nature Communications

https://doi.org/10.1038/s41467-026-72263-5

Article in Press

Structural and molecular basis of specialized translation mediated by the ribosome mRNA-binding channel

Received: 1 October 2025

Accepted: 6 April 2026

Cite this article as: Fraticelli, D., Hiregange, D.G., Weiss, B. *et al.* Structural and molecular basis of specialized translation mediated by the ribosome mRNA-binding channel. *Nat Commun* (2026). https://doi.org/10.1038/s41467-026-72263-5

Davide Fraticelli, Disha Gajanan Hiregange, Benjamin Weiss, Ariel Ogran, Tal Havkin-Solomon, Irene Martinez Roman, Anat Bashan, Ada Yonath & Rivka Dikstein

Structural and molecular basis of specialized translation mediated by the ribosome mRNA-binding channel

Davide Fraticelli[1]#, Disha Gajanan Hiregange[2]#, Benjamin Weiss[1], Ariel Ogran[1], Tal Havkin-Solomon[1], Irene Martinez Roman[2], Anat Bashan[2], Ada Yonath[2]*, Rivka Dikstein[1]*

[1]Department of Biomolecular Sciences, The Weizmann Institute of Science, Rehovot 7610001, Israel
[2]Department of Chemical and Structural Biology, The Weizmann Institute of Science, Rehovot 7610001, Israel

# These authors contributed equally

* These authors jointly supervised this work: ada.yonath@weizmann.ac.il; rivka.dikstein@weizmann.ac.il

Abstract

The ribosome mRNA channel is central to translation, yet its role in regulatory mechanisms remains unclear. Using cryo-EM of human ribosomal complexes bound to Kozak and TISU mRNAs from wild-type (WT) and RPS26/eS26 mutant (RPS26dC) cells, we demonstrate that both RPS26/eS26 and mRNA adopt distinct conformations, explaining their opposing effects on their activity. Translatome studies of WT and RPS26dC reveal AUG-context-dependent changes in 48S and 80S initiation complexes and slower scanning. Downregulated mRNAs are enriched for upstream AUG nucleotides and a -1-cytosine contacting 18S rRNA G1207, an interaction lost in RPS26dC. Strongly affected transcripts include replication-dependent histones, which, despite short 5'UTRs and suboptimal Kozak, exhibit robust translation activity that is RPS26/eS26-dependent. We identify a translational enhancer in the H2B 5'UTR (-16 to -9) overlapping predicted RPS26/eS26-binding sites, with a distinct ribosome-bound conformation. Exploiting these features, we engineered a high-efficiency translational cassette with reduced leaky scanning. These findings underscore the role of the ribosome's mRNA channel in selective translation and its therapeutic potential.

Introduction

The translation of mRNA is a critical stage in gene expression, playing a central role in all biological processes. This tightly regulated process allows cells to rapidly respond to environmental changes and developmental signals. Key regulators include factors involved in translation initiation, elongation, and termination, as well as specific mRNA features, predominantly located in the untranslated regions (UTRs). The translation efficiency of different mRNAs varies significantly and is influenced by the availability of specific eukaryotic initiation factors (eIFs), the presence of cis-elements within the 5' UTR, and the context surrounding the AUG start codon. Many of these components are modulated by major signaling pathways. The ribosome is integral to all stages of the translation cycle - initiation, elongation, termination, and recycling, and interacts dynamically with regulatory factors specific to each stage. Emerging research suggests that the ribosome itself can drive variations in translation. Such variations often stem from insufficient expression of specific ribosomal proteins (RPs), which is associated with genetic disorders like Diamond Blackfan Anemia (DBA), congenital asplenia, and 5q-syndrome. These diseases typically exhibit tissue-specific symptoms rather than widespread effects, indicating that abnormalities in translation are associated with the dysregulation of specific genes [1, 2, 3, 4].

Additional factors contributing to translational heterogeneity include RP paralogs (in yeast), post-translational modifications of RPs, chemical modifications of rRNA, proteins that are temporarily associated with the ribosome, and subcellular localization [5, 6, 7, 8, 9, 10]. These specialized ribosomal functions enable cells to fine-tune protein translation in a manner that meets cell-specific requirements. However, the full extent of ribosome-mediated regulation is not understood.

One underexplored regulatory mechanism inherent to the ribosome involves the ability of certain RPs within the small ribosomal subunit (40S, SSU) to interact directly with mRNA. Specific mRNA sequences along the mRNA path on the SSU may be preferentially recognized by these RPs, influencing the translation efficiency of differentially bound mRNAs. Although evidence for such regulation is limited, some studies suggest its potential, especially in the vicinity of the AUG start codon [11, 12]. However, most RP-mRNA interactions occur beyond the AUG start codon

region, and little is known about how these interactions relate to mRNA features or their role in translational control, especially in mammalian cells.

Recently, we conducted initial studies demonstrating the potential regulation of specific mRNAs by RPs in mammalian cells [13, 14]. Using site-specific genome editing in mammalian cells, we modified the amino acids contacting the mRNA of the endogenous RPS26/eS26 and RPS3/uS3, which are localized at the exit and entry channel of the 40S, respectively [13, 14]. The findings revealed differential effects on cap-proximal initiation, leaky scanning, and start codon fidelity. For RPS26/eS26, we unveiled the involvement of its C-terminal mRNA-binding tail in the translation regulation of specific mRNAs and its central role in integrating energy metabolism with the AMPK-mTOR signaling pathway [13]. However, the specific mRNA regulatory features involved and the underlying basis of these regulatory functions are unknown.

In this study, we investigated the structural basis and the regulatory landscape of the RPS26/eS26 mRNA binding in mammalian cells. Cryo-EM analyses of wild-type (WT) and RPS26/eS26-mutant (RPS26dC) ribosomal complexes bound to Kozak and TISU mRNAs revealed that RPS26/eS26 C-terminus adopts distinct conformations at the ribosomal exit channel with each mRNA, explaining its contrasting effects on their translation. Employing TCP-seq, TIS-seq, and Ribo-seq in WT and RPS26dC cells, showed sequence-specific rearrangements of both the key initiation intermediate 48S and the full 80S ribosomal complexes and slower scanning rates. Translationally downregulated mRNAs were enriched with specific AUG-upstream nucleotides, consistent with the mRNA positions that interact with the RPS26/eS26 C-terminus in each of the WT complex structures, and exhibited a high prevalence of a C at the -1 position that contacts 18S rRNA G1207. These interactions were lost in the mutant RPS26dC-ribosome structure. The most significantly downregulated mRNAs included replication-dependent histones, which are characterized by very short 5' UTRs and suboptimal Kozak elements, which typically correlate with poor translation efficiency. However, the 5' UTRs of histones H2B and H3 demonstrated strong translation activity, which relied on an RPS26/eS26-dependent enhancer located within mRNA nucleotides -16 to -9, i.e., the nucleotides predicted to interact with the RPS26/eS26 C-terminus. The structure of H2B 5'UTR-ribosome complex further supports differential mRNA binding conformation. On the basis of these unique features, we designed a translational cassette with

high efficiency and minimal leaky scanning, enhancing both efficacy and safety for mRNA-based therapies. These findings highlight the critical role of the ribosomal mRNA binding channel in selective translational regulation and its potential for advancing therapeutic applications.

Results

The structures of 80S ribosome bound to Kozak and TISU mRNAs reveal distinct conformations of the RPS26/eS26 C-terminus

We previously reported that the deletion of the C-terminal mRNA-binding domain of RPS26/eS26 (RPS26dC, amino acids 100-115) results in opposing effects on translation initiation directed by Kozak and TISU when preceded by a short 16 nt 5'UTR. However, when the leader was shortened to 10 nt, the effects of the mutation were lost [13]. au

The deletion of the last 15 C-terminal amino acids of RPS26/eS26 was confirmed using total and C-terminal specific antibodies as well as mass spectrometry (Supplementary Figure 1A and B). To understand the underlying basis of mRNA-specific effects of the ribosome, we employed cryo-EM on purified intact WT and RPS26dC 80S ribosomes assembled with Kozak and TISU mRNAs, bearing the same 16 nt leaders (Figure 1A), together with tRNAs as described in Materials and Methods and Supplementary Table 1 and the workflow shown in Supplementary Figures 2-5. We reached a resolution of 3.18 Å for the entire WT ribosome-Kozak mRNA complex and 3.02 Å for the WT ribosome-TISU-mRNA complex. The RPS26dC-ribosome-Kozak and the RPS26dC-ribosome-TISU complexes yielded final resolutions of 2.97 Å and 2.70 Å, respectively.

RPS26/eS26 interacts with upstream mRNA nucleotides within the exit channel. Cryo-EM density-guided model building of the C-terminal region of RPS26/eS26 in the WT and RPS26dC ribosomes, followed by structural superposition, confirmed the absence of residues 100-115 of the RPS26/eS26 C-terminus in the RPS26dC ribosome (Figure 1B). Analysis of WT ribosomes in complex with Kozak or TISU mRNA showed that the unstructured C-terminal tail of RPS26/eS26 up to P107 is stabilized in the presence of Kozak mRNA, contacting nucleotides -8 to -11, indicating a more stable interaction (Figure 1C-D). In addition to the C-terminal tail, RPS26/eS26 also contacts upstream mRNA through a conserved loop in the exit channel (Figure 1E). However, the functional interaction with nucleotides further upstream could not be observed. When bound to TISU mRNA, the C-terminal exhibited increased mobility, and its interaction with the -8 to -11 positions was not visualized, suggesting a weaker and less stable association (Figure 1G). In the RPS26dC ribosome bound to Kozak mRNA, the dimensions of the mRNA exit channel are markedly reduced and resemble those of the WT ribosome with TISU (Figure 1F and G). These findings align

with our previous functional studies demonstrating that in the context of a very short 5' leader, Kozak-driven initiation is highly dependent on RPS26/eS26 C-terminus interactions with the mRNA at the exit channel, while these interactions are inhibitory for initiation mediated by TISU [13].

Beyond the C-terminal tail, a loop of RPS26/eS26, particularly the Histidine residue at position 80 (H80), also interacts with the backbone of mRNA at positions -5 and -6 relative to the start codon of Kozak mRNA (Figure 1E). However, with TISU mRNA, the H80 interacts with the -4 mRNA base (Figure 1I), further highlighting the context-dependent differential mRNA binding. Remarkably, these H80-mRNA contacts are lost in RPS26dC ribosome-mRNA complexes (Figure 1J), suggesting an allosteric effect of the C-terminal tail on this interaction. Thus, in the context of Kozak mRNA, RPS26/eS26 establishes extensive interactions with AUG upstream nucleotides from positions -5 to -11 through both its C-terminal tail and H80. In contrast, fewer interactions were observed with TISU mRNA, providing a structural basis for the differential translational control mediated by RPS26/eS26 at the mRNA channel.

Translation initiation and elongation defects in RPS26 mRNA binding mutant cells

Despite the slow growth of the RPS26dC mutant cells, previous puromycin labeling experiments revealed no obvious difference between WT and RPS26dC mutant cells [13]. To further investigate a potential translation defect, we measured the rate of puromycin incorporation by treating an equal number of WT and RPS26dC cells with puromycin for 2.5, 5, and 10 minutes, followed by western blot analysis using anti-puromycin antibodies (Figure 2A). Although the signal after 2.5 minutes of treatment was similar between the two cell types, the rate of increase in the puromycin labeling over time was notably slower in the mutant cells (Figure 2A). As puromycin is a chain terminator, the slower increase in accumulation of puromycin-labeled peptides in the mutant cells suggests a reduction in initiation frequency or loading of new ribosomes. The comparable signal at the 2.5-minute puromycin pulse, despite the reduced initiation rate, suggests that elongating ribosomes are accumulating, presumably due to slower elongation.

To further elucidate the effect of the RPS26/eS26 C-terminal deletion on translation initiation, we investigated the scanning and AUG recognition stages by employing the Translation

Complex sequencing (TCP-seq) approach, which determines the position of the scanning 48S along the mRNA and at the initiation site. With this method, we isolated mRNA fragments protected by the 48S ribosome in WT and RPS26dC cells with two biological replicates. The reproducibility of the samples was confirmed by sample-wise clustering and correlation matrix (Supplementary Figure 6A). No differences were observed in the levels of rRNA, mRNA, or tRNA between the samples (Supplementary Figure 6B and C). Mapping the reads along the transcripts using metagene analysis revealed that most of the reads align to the 5'UTR, as expected from the scanning/initiating 48S ribosome (Figure 2B). However, the number of reads in the 5'UTR of the 48S ribosome of RPS26dC was much higher compared to WT, indicating an accumulation of the RPS26dC 48S complex during scanning. This finding is consistent with a slow movement of the scanning ribosome. Determination of the read length distribution shows a clear difference with a higher number of short reads in the mutant compared to the WT (Figure 2C), suggesting that the RPS26dC-48S complex has fewer contacts with the mRNA.

As a major fraction of the TCP-seq reads map to the initiation site, we examined the distribution of reads spanning the AUG by analyzing their exact boundaries at the 5' and 3' ends, as well as their length. In line with our previous findings [15], the ends of the reads are clustered at specific positions around the start site. The 5' and 3' end boundaries (Figure 2D, E and Supplementary Figure 6D), which reflect 48S protected fragments, accumulate at positions -12, +1, and -1, +24 respectively, in both WT and RPS26dC cells, exhibiting three major populations of reads (Figure 2F). We previously determined that the reads that end or start at the -1/+1 positions are the product of RNase I cleavage of the initiating 48S of the same transcripts [15]. The present data show a clear elevation of these -1/+1 reads in RPS26dC samples without a change in those ending at +24 (Fig. 2D and E), raising the possibility that the specific conformation of the initiation complex that is accessible to cleavage at this position is substantially prolonged in the mutant compared to WT. Investigating the initiation context associated with reads that are cut at position -1/+1, we found that in WT cells, these reads are associated with a weaker Kozak context due to the under-representation of +4G (Figure 2G). In contrast, these reads in RPS26dC cells are associated with a better Kozak context (Figure 2G), suggesting that the RPS26dC 40S complex is less stable even when initiating at a strong context. Additionally, in both WT and mutant cells, the

C in position -1 is remarkably enriched, as previously reported [15]. No differences were observed between the initiation contexts of WT and mutant for uncleaved reads (Supplementary Figure 6E).

We next analyzed the length of reads that end at +19 and approximately +24 from their 3' ends. In WT cells, there is an accumulation of 37nt and 47nt reads (Figure 2H, grey). The 37nt reads correspond to mRNA fragments that are entirely protected by the ribosome from RNAse I cleavage, while the extended 47nt reads represent those protected by both the ribosome and eIF3, as previously described [15]. In contrast, the largest accumulated population in RPS26dC cells is of 24nt long reads, which indicates cleavage by RNase 1 at position -1 relative to the AUG. This finding further confirms a prolonged duration of the initiation complex in this specific conformation in RPS26dC cells (Figure 2H, red). Notably, immediately downstream of the AUG, there are several peaks that are exactly 3 nucleotides apart from each other, especially in the mutant samples (Figure 2E). These intervals are consistent with 48S complexes that are slowly progressing behind a slower initiating/elongating 80S ribosome. This lagging provides RNAse I the time to cleave specifically after every 3 nucleotides, according to the movement of the elongating 80S ribosome (Figure 2I).

To determine whether the altered association of initiation factors contributes to the observed initiation defects, we analyzed by mass spectrometry the levels of eIFs associated with the 40S subunit in WT and RPS26dC mutant cells. The analysis revealed no significant differences in the abundance of any initiation factors, including eIF3a, which is located in close proximity to RPS26 in the pre-initiation complex (Supplementary Table 3).

The size of ribosome occupancy at the initiation site is context- and RPS26/eS26-dependent

To further examine the impact of impaired mRNA binding by RPS26/eS26 on translation, we performed ribosome profiling [16] with Cycloheximide (CHX) to monitor translation efficiency (Ribo-seq) and with Harringtonine (HAR) combined with CHX to stall the initiating ribosome, enabling the assessment of translation initiation (TIS-seq). In parallel, total RNA was extracted from the same samples and subjected to RNA-seq. The reproducibility of the replicates was confirmed by sample-wise clustering and correlation matrix (Supplementary Figure 7A). The libraries displayed

high similarity in the medians of the normalized sample reads counting (Supplementary Figure 7B) as well as in read length per open reading frame (Supplementary Figure 7C). The analysis of reads distribution along transcripts using metagene analysis showed that in the Ribo-seq samples (Figure 3A, left), the reads are distributed at the initiation site and all along the coding region (CDS), while in the TIS-seq samples, most of the reads are clustered near the ORF start and not the CDS, as expected (Figure 3A, right). However, the read counts around the AUG and the coding regions are substantially lower in the RPS26dC mutant cells compared to the WT in both Ribo-seq and TIS-seq, suggesting impairments in both translation initiation and elongation.

The basis of Ribo-seq is the protection of the translated mRNA by the ribosome mRNA channel. Under physiological conditions, the length of the mRNA protected by the ribosome is around 28-30 nt, and the library is generated from 26 to 32 nt mRNA-protected fragments. Interestingly, the count per read length of the Ribo-seq samples showed a substantial increase of 27 nt long reads, accompanied by a reduction of 29 and 30 nt long reads in RPS26dC compared to the WT cells (Figure 3B). Metagene analysis of each read length showed that with the 27 nt reads, the upregulation in RPS26dC is seen both at the start site and the CDS (Figure 3C). In contrast, in the longer 29 nt reads, both the initiation and CDS are diminished, while in the 28 nt footprints, only the CDS reads are reduced (Figure 3C). These findings are in line with overall reduced mRNA contacts during both initiation and elongation in RPS26dC mutant.

Next, we used the TIS-seq data to assess the length of ribosome occupancy at initiation sites and whether the range of protection is transcript-specific. To this end, we identified the initiation reads in each transcript and determined their length. A specific read length was assigned to a transcript if it appeared in more than 50% of the transcript reads in at least 2 of the 3 replicates. This analysis showed that, indeed, 30% of the mRNAs can be grouped according to the size of ribosome protection at the initiation (Figure 3D). Notably, those with predominant 29 and 30 nt initiation read lengths were significantly reduced in the RPS26dC samples (Figure 3D). To elucidate the basis of this length-dependent vulnerability, we examined the initiation context associated with each read length. This analysis reveals that in both WT and mutant samples, transcripts with ribosome initiation site protection of 27 nt differ from those with 28 nt by the presence of a G at the +4 position, which is under-represented in the 27 and enriched in the 28

nt reads (Supplementary Figure 7D and E). Additionally, the longer 29 nt reads are notably enriched with C/G at the -9 position (Supplementary Figure 7D, E), suggesting the importance of this nucleotide position in generating extended footprints and the stability of the initiating ribosome. The occurrence of the -9 C/G in the longer reads that are particularly sensitive to the RPS26/eS26 C-terminal deletion (Figure 3B and D) is intriguing, as the C-terminal tail interacts with this region (Figure 1B) and likely contributes to translation initiation stability.

The finding that the size of ribosome protection is linked to specific transcripts bearing defined initiation context prompted us to examine whether these transcripts belong to specific biological functions. Using the ShinyGo engine [17], we found highly significant enrichment of specific categories with minimal overlap between the functions of transcripts with different read lengths (Supplementary Figure 8). Collectively, these findings suggest that the effect of RPS26dC on translation initiation is both sequence- and transcript-specific.

To determine the impact of RPS26dC on translation efficiency, we calculated the ratio of the reads per transcript from the Ribo-seq data to the total mRNA levels from the RNA-seq data. Our findings revealed that 309 transcripts were downregulated and 184 transcripts were upregulated by at least 1.7 fold in the mutant compared to the WT cells (Figure 3E). We then compared the AUG initiation contexts of upregulated, downregulated, and unchanged transcripts between WT and RPS26dC cells (Figure 3F). Notably, when compared to the unaffected transcripts, a C at position -1 relative to AUG is highly prevalent in the downregulated transcripts (Figure 3F). This finding is intriguing, as this C is also enriched in the transcripts showing enhanced RNase I cleavage at -1/+1 in the TCP-seq data (Figure 2G). We, therefore, looked at this position in the ribosome-mRNA structure. Interestingly, we observed that the interaction between 18S rRNA nucleotide G1207 and the -1 position of both Kozak and TISU mRNAs is dramatically distorted in the RPS26dC ribosome compared to the WT (Figure 3G-I and supplementary Figure 9A). Specifically, in WT ribosomes, G1207 engages in a precise stacking interaction with the -1 nucleotide of both Kozak and TISU mRNAs (Figure 3G and 3H). However, in the RPS26dC ribosomes, the interaction is shifted, with G1207 forming a new contact with the -2 position in the Kozak complex and the -5 position in the TISU complex (Figure 3I and Supplementary Figure 9A), while the lack of interaction with the -1 position leads to the flipping out of this nucleotide.

Overall, these findings further support a model in which RPS26/eS26 contributes to initiation complex stability through sequence-specific interactions at the mRNA exit channel.

We then investigated the potential impact of the 5'UTR length on the observed changes in translation and found no significant difference between the downregulated and unchanged transcript sets (Supplementary Figure 9B). Next, we used the TIS-seq data to analyze the number of active initiation sites in the 5'UTRs (active uORFs) and compare the prevalence of active uORFs among the affected and non-affected mRNAs. The results revealed a decreased and increased prevalence of uORFs among the downregulated and upregulated mRNAs, respectively (Supplementary Figure 9C), suggesting a possible role of the RPS26/eS26 C-terminus in modulating leaky scanning or reinitiation (see below). Altogether, these findings uncover the importance of the translation initiation sequence features in the extent of ribosome occupancy and the central role of RPS26/eS26 C-terminal mRNA binding in the stability of the ribosome in vivo.

The ribosome mRNA binding channel drives a specialized translation enhancer of histone mRNAs

To further study the mRNA-specific regulatory functions of RPS26/eS26 in mRNA binding activity, we analyzed the biological functions and gene categories of RPS26dC-affected mRNAs using the ShinyGo tool [17]. Among the most significantly enriched pathways, Nucleosome Assembly and Chromatin Organization showed the highest statistical significance (Figure 4A). These categories include multiple replication-dependent histone genes as the most downregulated transcripts (Figure 4A and Supplementary 10A). To confirm these findings, we subjected the WT and RPS26dC cells to polysome profiling and then compared the levels of histone mRNAs between heavy and light fractions in WT and RPS26dC cells by RT-qPCR. Consistent with the Ribo-seq results, H1, H2B, and H3 mRNA levels were significantly reduced in RPS26dC compared to the WT, while H4 translation remained unchanged (Supplementary 10B). Histone genes are characterized by an exceptionally short 5'UTR (Figure 4B) and a weak AUG context (Figure 4C), features that are known to promote leaky scanning and inefficient translation. Additionally, these mRNAs are regulated by a stem-and-loop at their 3'UTR bound by the Stem-Loop Binding Protein (SLBP) [18].

Despite these constraints, large amounts of histone mRNAs and proteins are synthesized during S-phase to build the duplicated chromatin. While the translation of histone H4 has been studied in some detail [19], the regulation of the other histones remains unexplored. To investigate the mechanism of histone translational control and the underlying basis of their RPS26/eS26 C-terminus dependency, we focused on the initiation phase. We first analyzed the AUG context of affected and unaffected histone mRNAs and found it to be unchanged (Figure 4C), suggesting that the initiation context is less likely to be involved in RPS26/eS26 C-terminus-dependent regulation. We next used the TIS-seq and Ribo-seq data to compare the read count distribution across different read lengths. While there is an overall increase in the 27 nt reads and a reduction of 29 nt and 30 nt reads in all genes, these effects are more pronounced in the TIS-seq data for histone mRNAs (Figure 4D) while the length distribution of the elongating 80S is similar (Supplementary Figure 10C and D), suggesting a particular initiation impairment of histone mRNAs. Then, we performed metagene analysis of the TCP-seq data of histone mRNAs in WT and RPS26dC cells, focusing on the position of the last nucleotide at the initiation site. This analysis revealed that histone genes displayed several heightened peaks along the 5'UTR exclusively in RPS26dC cells, indicating much greater accessibility to cleavage by RNase 1 in the mutant cells (Figure 4E). Collectively, these findings suggest that RPS26/eS26 C-terminus forms extensive contacts with the histone 5'UTR upstream of the AUG.

To investigate further how RPS26/eS26 C-terminus regulates histone mRNA translation, we utilized reporter genes in which the firefly luciferase is controlled by various regulatory features (Figure 4F, left). The first construct is a control with an unstructured 5'UTR of 100 nt and a Kozak context (CTR-K), the second is identical except it contains the weak AUG context of the H2BC4 (CTR-W). The third features 5'UTR of H2BC4 (22nt) along with its sub-optimal AUG context (H2B-5'UTR), the fourth is the H2B 5'UTR with the strong TISU-like context, and the fifth uses the same 5'UTR as the CTR-K, but its 3'UTR was replaced by the histone 3'UTR, and the last is the H3 5'UTR (34 nt). The activity of these constructs was analyzed in WT and RPS26dC mutant cells (Figure 4F, right).

Surprisingly, despite the very short 5'UTR and weak AUG context, the activity driven by the H2B-5'UTR as well as the H3 5'UTR constructs in WT cells was ~two-fold higher than the

control CTR-K bearing optimal 5'UTR length and AUG context. These findings suggest the presence of a translation enhancer within the histone 5'UTRs. While the CTR-K and CTR-W activities were elevated in RPS26dC, that of the H2B and H3 5'UTRs was significantly reduced in the mutant cells, suggesting that the histone enhancer is dependent on RPS26/eS26 C-terminus (Figure 4F, right). Strengthening the AUG context as in H2B-TISU-like, retained RPS26/eS26 C-terminus dependency (Figure 4F, right), confirming that RPS26/eS26 C-terminus controls the H2B-5'UTR enhancer rather than the AUG context. Finally, the presence of histone 3'UTR similarly inhibits translation efficiency in both WT and RPS26dC (Figure 4F, right). To confirm that the observed effect of RPS26/eS26 on histone 5'UTRs occurs at the translation level, we in vitro synthesized and capped the same H2B 5'UTR-firefly luciferase fusion mRNA and transfected it into WT and RPS26dC cells. Similar to the plasmid transfection results, the normalized luciferase activity of the histone 5'UTR in RPS26dC mutant cells is lower than the WT cells (Figure 4G).

Considering the importance of positions -10 to -16 for the effect of RPS26/eS26 C-terminus on Kozak and TISU [13], we tested the significance of these positions for the translational enhancer of the histone 5'UTR by shortening the 22 and the 34 nt long 5'UTR of H2B and H3 to 16 and 10 nt. In both H2B and H3 5'UTRs, the reporter activity of the 10-nucleotide-long 5'UTR was significantly lower compared to the 16 nt in WT cells, while the effect of this deletion was insignificant in RPS26dC mutant cells (Figure 4H and I). These findings raise the possibility that the enhancer lies within this segment. To further characterize the H2B 5'UTR, we focused on the U nucleotides in positions -5, -6 that are more prevalent in the affected histone mRNAs compared to the non-affected ones (Figure 4C) and introduced mutations at these positions (Mut -5/-6). In addition we mutated the (-9)-(-16) region and combined both mutations Mut -5/-6 plus (-9)-(-16)), as depicted in Figure 4J. In addition, we mutated the highly conserved C at position +5. Mutations at the -5/-6 or the +5 positions had no significant effect on the enhancer activity (Figure 4J, middle), however, the (-9)-(-16) mutations dramatically reduced the reporter activity in WT and mutant cells (Figure 4J, middle). The combined -5/-6 plus (-9)-(-16) mutant had no additive inhibitory effect relative to each mutation alone (Figure 4J, middle). Thus, the region spanning -9 to -16 is the most critical for the enhancer activity. We compared the extent of inhibition of the (-9)-(-16) mutations in the WT and RPS26dC cells and found it to be lower in the mutant cells

(Figure 4J, right). Altogether, these results uncovered the -9 to -16 nucleotides as an important regulatory sequence involving RPS26/eS26 C-terminus in its function.

Structural insights into RPS26/eS26 C-terminus interaction with H2B mRNA

To elucidate further the translation directed by histones 5'UTR, we employed cryo-EM on WT 80S ribosome assembled with H2B mRNAs (as described in Materials and Methods, the workflow in Supplementary Figure 11A and Supplementary Table 1), yielding a high-resolution structure of 2.41 Å for the 80S ribosome. Notably, the 5' end of the H2B mRNA was visible up to position -5, with partial stabilization of RPS26/eS26 C-terminus extending to residue 103, suggesting an interaction interface between the histone leader and the ribosome. While the enhancer region located further upstream (-9 to -16) remained unresolved (Figure 5A-B), likely due to transient or dynamic interactions, RPS26/eS26 H80 flipped from a phosphate-backbone contact seen with Kozak mRNA to a base-stacking interaction with nucleotide -4 in the H2B mRNA (Figure 5C). Conserved interactions at the decoding center, such as the -1 nucleotide of mRNA pairing with 18S rRNA G1207, are also seen here (Figure 5D). Superimposition of mRNA exit-channel ribosomal proteins (RPS2/uS5, RPS14/uS14, RPS26/eS26, RPS28/eS28) from Kozak, TISU, and H2B complexes reveals that the RPS26/eS26 C-terminus adopts different conformations depending on the 5'UTR context (Figure 5E-H). These differences support a model in which the RPS26/eS26 C-terminus dynamically adjusts its conformation to modulate ribosome configuration and translation initiation in an mRNA-specific manner, either reinforcing stabilization or remaining permissively unstructured depending on the nature of the 5'UTR (Figure 5E-H).

RPS26/eS26 C-terminus has an opposite effect on leaky scanning depending on the 5'UTR length

To determine the potential involvement of uORFs in translation in RPS26dC mutant cells, we assessed the effect of active uORFs on translation efficiency in WT and mutant cells and found no significant difference (Supplementary Figure 12A). We also analyzed the frequency of uORFs among the down- and upregulated mRNAs compared to the unchanged transcripts and

confirmed that uORF presence is not correlated with reduced translation (Supplementary Figure 12B).

Short 5' UTRs are commonly associated with leaky scanning (LS) [20]. We, therefore, investigated whether leaky scanning is altered in RPS26dC mutant cells. Using the TIS-seq data, we analyzed the number of transcripts that exhibited either reduced or elevated LS in RPS26dC mutant cells relative to WT cells by calculating the ratio between reads that their P-site mapped to the expected location (+1 to +3) to those that were mapped immediately downstream (+4 to +30). An increase or decrease in this ratio indicates enhanced or reduced LS, respectively. We then analyzed the 5'UTR length of transcripts with either increased or decreased LS in the RPS26dC mutant relative to WT cells (Figure 6A). Notably, transcripts with short 5' UTRs demonstrated increased LS in mutant cells, while transcripts with long 5' UTRs showed the opposite trend (Figure 6A). To further investigate the regulation of translation initiation fidelity of histone 5'UTR by RPS26/eS26 C-terminal tail, we generated constructs in which the 22 or 34 nt long H2B and H3 5'UTRs, respectively, including their AUG flanking sequence, are 31 nt away (and therefore out of frame) from a second AUG in a Kozak context that is in frame with the Fluc reporter (H2B-LS, H3-LS, respectively). This way the luciferase activity reflects the outcome of leaky scanning (see scheme in Figure 6B). WT and RPS26dC mutant cells were transfected with the original H2B and H3 5'UTRs and their LS counterparts, and the ratio between the two was determined (Figure 6B and Supplementary Figure 12C and D). Both the H2B and H3 5'UTRs exhibit a significant level of LS. However, the H2B LS was further elevated in the mutant cells while that of H3 is unaffected (Figure 6B), suggesting that the RPS26/eS26 C-terminus effect is 5'UTR length dependent.

Next, we utilized the control plasmid described above (CTR-K) to generate two additional Fluc constructs in which an upstream AUG is placed 47nt (out of frame) from the original AUG that drives the Fluc (Figure 6C, CTR-LS) and marks leaky scanning events. In the second, an upstream AUG is followed by an in-frame stop codon, enabling the measurement of re-initiation events (Figure 6C, CTR-RI). Transfection of the parental CTR-K, CTR-LS, and CTR-RI plasmids into WT and RPS26dC cells revealed a reduced leaky scanning in mutant cells compared to WT cells (Figure 6C, and Supplementary Figure 12E) which is the opposite of the effect seen with the H2B

5'UTR. On the other hand, the extent of reinitiation in WT and mutant cells is comparable. These findings are in full agreement with the 5'UTR length-dependent LS calculated from the Ribo-seq results (Figure 6A). The reduced leaky scanning from long 5'UTR is most likely a consequence of the slow progress of the 48S.

Engineering of an expression cassette based on H2B-5'UTR for high translation and minimal leaky scanning

The use of mRNA as a vaccine and for other therapeutic applications involves its introduction into the human body, where it is translated into functional protein. This application faces significant challenges that impact its efficacy and safety, including the size of mRNA molecules to be encapsulated for delivery and the efficiency of translation [21, 22]. Another critical limitation is the safety of the translated products, as even low levels of leaky scanning can lead to the production of truncated or non-functional proteins as well as undesired alternatively initiated peptides that raise safety concerns [21]. To address these limitations, we aimed to exploit the translational enhancer of the short 5'UTR of H2B and further develop it to achieve strong expression with minimal leaky scanning by generating the constructs shown in Figure 6D. As the H2B AUG context is suboptimal, we replaced it with a TISU-like context known for its ability to reduce leaky scanning from a very short 5'UTR [23, 24]. Likewise, we introduced the canonical TISU element with either a C or G and the -4 position. For each of these AUG contexts, we paired a similar plasmid that can report leaky scanning as described for H2B-LS in Figure 6B. The presence of the TISU-like and TISU contexts maintained high translation activity while significantly reducing the leaky scanning to an extent similar to long 5'UTR (Figure 6D and F). To further reduce the potential to generate alternatively initiated peptides, we generated plasmid pairs in which the TISU start is followed by another in-frame AUG, so the residual leaky scanning will initiate from it and avoid the generation of undesired products. Indeed, measuring the extent of leaky scanning past this second AUG confirms that it is negligible (Figure 6E and F). Thus, this configuration reduced LS to the minimum and the potential to produce meaningful quantities of alternative peptides.

Discussion

In this study, we integrated structural and molecular studies to elucidate selective translational control mediated by the ribosome mRNA channel. Focusing on the C-terminal tail of RPS26/eS26 mRNA binding domain at the exit channel, we provide structural and functional evidence for the direct involvement of its mRNA binding in the translation regulation of specific mRNAs, along with the associated regulatory features. These include the differential interaction of RPS26/eS26 C-terminus with Kozak, TISU, and H2B 5'UTR and the importance of this domain in orienting additional mRNA interactions such as H80 with -4 and -5 positions and 18S rRNA G1207 interaction with the -1 position relative to the AUG. In the absence of the C-terminus, these additional interactions are lost. These findings closely align with the translatome experiments demonstrating that affected mRNAs are enriched with specific nucleotides at exactly the same positions.

By employing several global methodologies, we provide compelling evidence that RPS26dC mutant cells exhibit defects in translation initiation and elongation. Kinetics of puromycin labeling rates indicate that the accumulation of puromycin is slower in mutants, suggesting impairments in both stages of translation. TCP-seq analysis further shows an accumulation of 48S complexes in the 5' UTRs, pointing to delays in ribosome scanning as well as lagging behind slow elongating ribosomes. The scanning defects are likely a consequence of reduced mRNA binding. Taking into consideration that RPS26dC cells have a reduced ATP/ADP ratio compared to WT cells [13, 25], it is also possible that limited energy supply affects the activity of RNA helicases that facilitate the scanning process, such as DDX3X and eIF4A [25, 26]. Additionally, read-length analysis indicates an increase in short 48S-protected fragments, confirming diminished ribosome-mRNA interactions in the absence of the RPS26/eS26 C-terminus and instability of the initiation complex.

Ribo-seq and TIS-seq analyses further revealed that RPS26dC mutant cells have reduced ribosome occupancy both at translation initiation sites and along coding regions, as well as a shift toward shorter 27 nt ribosome-protected fragments and a decrease in longer 29–30 nt footprints. These reduced ribosome-mRNA interactions involve transcripts with specific features, such as GC-rich sequences upstream of the start codon and particular enrichment of a C at the -1 position, a

feature linked to the enhanced RNase I cleavage in the TCP-seq data and the interaction of 18S rRNA G1206 with this position which is lost in the mutant, according to the structural data. These results highlight the importance of the RPS26/eS26 mRNA binding activity in the translation of specific mRNAs bearing defined features.

Our experiments led to the identification of the replication-dependent histone mRNAs as primary targets of RPS26/eS26 mRNA binding. These mRNAs display several unique features that include the lack of introns and polyA tails, unusually short 5' UTRs, suboptimal Kozak elements, and a regulatory 3'UTR stem-loop structure [27, 28, 29]. All these features are known to correlate with poor translation efficiency. Nevertheless, during the S-phase, large amounts of newly synthesized histones are produced for the duplicated chromatin. Our findings provide insights into the mechanisms enabling histone mRNAs to be effectively translated despite these seemingly inhibitory features. The 48S footprints around the start site of the affected histone mRNAs revealed substantial contacts of the RPS26/eS26 C-terminus with the 5'UTR of histone mRNAs. Furthermore, both H2B and H3 5' UTRs demonstrated strong translation activity that relies on the RPS26/eS26 mRNA binding. Mutational analysis identified the -9 to -16 nucleotide region as critical for this enhancer function in both H2B and H3. A previous study reported a special role of eIF3 in the binding and translation of histone mRNAs [24, 30]. It would be interesting to examine whether eIF3 subunits cooperate with the ribosome mRNA channel to regulate histone mRNA translation through the translational enhancer identified here.

Both the former and current studies highlight the importance of positions -9 to -16 in the regulation of short leaders mRNAs by the Rps26/eS26 C-terminus. Specifically, the opposing effects of the RPS26dC on Kozak and TISU initiators were lost when their 5'UTR was shortened from 16 to 10 nt [13]. Likewise, mutating positions -10 to -16 in the H2B and H3 5'UTRs reduced the enhancer activity and diminished the effect of RPS26dC, uncovering its importance for position-specific regulatory sequences. The translatome studies of both 48S and 80S ribosomal complexes revealed loss of ribosome contacts with this region. However, these mRNA positions, as well as the RPS26/eS26 C-terminal end (amino acids 108-115), are not resolved in the cryo-EM ribosome-mRNA structures reported here, likely due to their flexible or dynamic interactions. This observation highlights the limitations of structural approaches in capturing dynamic elements of

translation regulation and suggests that future studies with cross-linking or ribosomal stalled complexes may help visualize and characterize this unstructured interface and its contribution to selective mRNA translation.

The finding that the RPS26/eS26 C-terminus is dispensable for the Kozak element in long, scanning-dependent translation (this study and [13] does not align with studies in yeast, which report that RPS26/eS26 is important for the translation efficiency of Kozak mRNAs [31]. This discrepancy is likely due to the fact that the yeast studies examined complete RPS26/eS26 depletion, whereas in our experimental system, only the C-terminal domain of RPS26/eS26 is deleted.

By combining insights from Ribo-seq and reporter assays, RPS26/eS26 C-terminus was found to play a critical role in preventing leaky scanning, particularly of transcripts bearing short 5'UTRs, which could have significant implications for the translation of histone and other transcripts driven by short 5'UTRs**.** In contrast, long 5'UTRs show reduced LS compared to WT, while re-initiation levels remained unchanged, suggesting that RPS26/eS26 C-terminus specifically modulates translation initiation fidelity rather than ribosome reinitiation. The leader-length dependency of the leaky scanning effect can be explained by the differences in the initiation mechanism. Initiation from AUGs preceded by short 5'UTR, is characterized by insufficient contacts at the ribosome exit channel as well as potential steric clash between the ribosome and the cap-bound eIF4F [23, 24, 32], rendering it more sensitive to the destabilizing effect of RPS26dC mutation. Given that leaky scanning poses a significant safety concern in the translation of therapeutic mRNAs [21], we utilized the unique features of H2B 5'UTR to design translational cassettes that display high translation efficiency and minimal leaky scanning for the potential use in mRNA-based therapies. Overall, these findings highlight a novel regulatory role of RPS26/eS26 mRNA binding in histone gene expression, which may be crucial for maintaining proper chromatin assembly during the cell cycle and have implications for therapy.

Building on the findings of this study, we envision that the potential of ribosome-specific translation regulation, mediated by ribosomal proteins positioned within the mRNA channel, is only beginning to be uncovered. Future research into these regulatory mechanisms could deepen

our understanding of translational control and reveal novel therapeutic targets for advancing human health.

Limitations of the study

The cryoEM experiments clearly show reduced mRNA binding by Rps26dC mutant ribosomes, but do not provide a quantitative estimate of the change in the binding affinity.

Our 80S-mRNA-Met-tRNA complexes best represent the ribosome at the end of initiation (Supplementary 13B), prior to the first elongation step. Nonetheless, these structures capture key mRNA–ribosome interactions that persist from earlier stages of initiation. The pre-initiation (48S) complexes differ in both composition and conformation, particularly due to the presence of initiation factors such as eIF3, eIF1, and eIF1A, which occupy regions near the mRNA entry channel and the RPS26/eS26 site. The recent 48S structure reported by [33] revealed that RPS26/eS26 C-terminal tail is already positioned adjacent to the region of mRNA even before 60S joining (Supplementary 13C, D), suggesting that the interactions we observed in the 80S complex likely represent a stabilized continuation of contacts established during scanning and start site selection. Particularly, the presence of eIF3a near RPS26/eS26 C-terminus and other initiation factors in the 48S state could modulate these interactions. We therefore interpret our 80S structures as providing a structural endpoint model that complements rather than replaces direct views of scanning intermediates.

Although the TCP-seq data are of high quality and the replicates are highly consistent, the limited number of biological replicates (2) may restrict the statistical power of the data.

Methods

Purification of ribosomes from human embryonic kidney cells (HEK293T)

Ribosomes were purified from both WT and RPS26dC HEK293T cells that were previously described [13]. Cells were grown at 37º C in a humidified incubator with 5% CO2 in Dulbecco's modified Eagle's medium (Gibco, Life Technologies, Thermo Scientific, Waltham, MA, USA) supplemented with 10% fetal bovine serum (FBS; Gibco), 100 units/ml penicillin and 100 µg/ml streptomycin. Cells were scraped, washed with ice-cold PBS, and pelleted by centrifugation at 900 rpm for 10 min. Cell pellets were resuspended in ice-cold PBS and repelleted via centrifugation. Cells are then lysed in freshly prepared lysis buffer A containing 30 mM Tris, pH 7.5, 2% TritonX-100, 20 mM MgCl2, 300 mM NaCl, RNAsin (Promega) and 1X CoMplete Mini protease inhibitor cocktail. Cells were mixed gently by multiple inversions of the culture tube and incubated on ice for 10 min to complete lysis. Cell lysates were cleared of debris and nuclei via centrifugation at 9500 rpm at 4° C for 10 min. The supernatant was loaded on 1.1M sucrose cushion prepared in buffer B (45 mM HEPES KOH, pH 7.5, 150 mM KOAc, 10 mM Mg(OAc)2, and 2mM DTT) and centrifuged for 16 h at 55000 rpm to get the crude ribosomal pellet. Sucrose cushion buffer was treated with bentonite after preparation to inhibit ribonucleases. The pellet was resuspended in Buffer C (20 mM Tris pH 7.5, 150 mM KOAc, 10 mM Mg(OAc)2, RNAsin, and 2mM DTT) to homogeneity, and particles were removed by short centrifugation (10 min at 9500 rpm) and the supernatant was loaded on a linear gradient of 10-40% sucrose. The sucrose buffer was treated with bentonite after preparation to inhibit ribonucleases. The samples were centrifuged at 22,000 rpm for 11 h in a SW-28 rotor, fractions were collected and absorbance (A260) was measured for each. Fractions corresponding 80S peak were pooled together and further centrifuged at 56,000 rpm for 16h at 4℃. The pellet was suspended in Buffer D [20 mM Tris pH 7.5, 100 mM KOAc, 10 mM $Mg(OAc)_2$, 10 mM NH4OAc and 1 mM DTT], centrifuged for 2.5 h at 75,000 rpm (Ti100 rotor, Beckman). The pellet was dissolved in Buffer D overnight without shaking. The dissolved pellets were flash frozen in aliquots and stored at -80^{0}C.

mRNA-tRNA-ribosome complex formation

Ribosome complexes with mRNA, three tRNA molecules and Hygromycin were assembled by sequentially adding a Kozak mRNA fragment (AGAUCCGCUAGCGGGAAUGUGGAGAGA, Sigma), or a TISU mRNA fragment (AGAUCCGCUAGCCAAGAUGGCGGCAGA, Sigma), or a H2B mRNA fragment (UUUCUGGUGUUUUAAGAUGCCGGAGUC, Sigma). Following this, tRNA mixture (Sigma) and Hygromycin were added in a stoichiometric ratio of 1:100:5:100. Hygromycin was added to stabilize the mRNA-tRNA-ribosome complex formation (Supplementary 13A). The complex assembly was performed at 26°C in ribosome storage buffer (20 mM Tris pH 7.5, 100 mM KOAc, 10 mM $Mg(OAc)_2$, 10 mM NH_4OAc and 1 mM DTT), with relaxation times of 30 minutes after the addition of each component.

Cryo-EM sample preparation and data collection of ribosomes

Human 80S ribosomes were applied onto glow-discharged holey carbon grids coated with a continuous thin carbon film. Grids were blotted and plunge-frozen using a Vitrobot Mark IV (Thermo-Fischer Scientific) with parameters set as follows: sample volume 3.5 µl, blot time 2.5 sec, wait time 30 sec, and blot force -1. Cryo-EM micrographs were acquired at liquid nitrogen temperature using a Titan Krios electron microscope (Thermo-Fischer Scientific) operating at 300 kV, equipped with a K3 direct electron detector (Gatan Inc.) at a nominal magnification of 105K and a pixel size of 0.842 Å/pixel for WT ribosomes with Kozak and TISU mRNAs, and 0.824 Å/pixel for H2B mRNA as well as for RPS26dC ribosomes with Kozak and TISU mRNAs, respectively. Defocus values ranged from -0.5 to –1.5 µm.

Cryo-EM data processing and refinement of ribosome structures

Data processing was conducted using RELION 4.0 and RELION 5.0 [34], with motion correction performed using Motioncor2 [35]. Contrast transfer function (CTF) parameters were estimated using CTFFIND-3 [36]. Initial 3D models were built using semi-automatic particle picking and reference-free 2D classification. Particles selected from 2D classification were subjected to 3D auto-refinement, followed by 3D classification without alignment to sort for structurally distinct populations. Particles showing clear density for mRNA and tRNA were further refined through CTF refinement, particle polishing, and additional rounds of 3D refinement to obtain a high-resolution density map [37]. Subsequently, to account for flexibility between ribosomal subunits,

we performed multibody refinement in RELION using separate masks for the 40S and 60S subunits. [38]. For each body, the refinement parameters included the mask, the reference body for relative rotation, the standard deviation of allowed angular rotations, and the standard deviation of allowed translational shifts (e.g., 40S body: reference = 1, sigma angles = 10, sigma offset = 2. 60S body: reference = 2, sigma angles = 10, sigma offset = 2). This allowed independent alignment of each subunit while maintaining overall 80S coherence and improving local resolution in flexible regions such as the mRNA channel and inter-subunit interfaces.

For the cryo-EM structure of WT-Kozak mRNA ribosome complex, initial data yielded a 4.2 Å resolution reconstruction of the entire ribosome from 168617 particles. Following this, 3D classification without alignment was performed to sort the population of tRNA-mRNA-bound ribosomes from vacant ribosomes. After 3D-sorting, 55958 particles were used for reconstruction with a resolution of 4.2 Å. Subsequent CTF refinements and polishing improved the resolution to 3.74 Å. To further improve the resolution, multi-body refinement was performed, which subsequently led to an improved resolution of 3.18 Å for the entire ribosome, specifically 3.15 Å for the LSU and 3.25 Å for the SSU (Supplementary Figure 2 and Supplementary Table 1). Likewise, for the WT ribosome-TISU-mRNA complex cryo-EM structure, initial data processing yielded a 4.0 Å resolution reconstruction of the entire ribosome from 134909 particles. After sorting, 74646 particles were used to achieve a 3.8 Å resolution reconstruction. Further, CTF refinement and particle polishing improved the resolution to 3.29 Å. To further improve the resolution, multi-body refinement was applied, resulting in a final resolution of 3.02 Å for the entire ribosome, with 2.99 Å for the LSU and 3.06 Å for the SSU (Supplementary Figures 3 and Supplementary Table 1). For the cryo-EM structure of RPS26dC-ribosome-Kozak mRNA complex, the dataset included 99,817 particles, resulting in a 3.55 Å resolution reconstruction. A 3D classification without alignment was subsequently conducted to distinguish between the tRNA-mRNA-bound ribosomes and vacant ribosomes. After sorting, 59189 particles were used to achieve a 3.58 Å resolution reconstruction. Further refinement and multi-body refinement improved the resolution to 2.97 Å for the entire ribosome, with specific resolutions of 3.09 Å for the LSU and 3.16 Å for the SSU (Supplementary Figure 4 and Supplementary Table 1). For determining the RPS26dC-ribosome-TISU complex structure, the dataset comprised 96017 particles, yielding a 3.1

Å resolution reconstruction. A 3D classification without alignment was then performed to differentiate between the tRNA-mRNA-bound ribosomes and vacant ribosomes. Following sorting, 50884 particles were used to produce a 3.1 Å resolution reconstruction. Subsequent refinement, including multi-body refinement, further improved the resolution to 2.70 Å for the entire ribosome, with specific resolutions of 2.70 Å for the LSU and 2.90 Å for the SSU. (Supplementary Figures 5 and Supplementary Table 1).

For the cryo-EM structure of WT ribosome-H2B-mRNA complex, initial data processing of 142,054 particles yielded a 3.2 Å resolution reconstruction of the entire ribosome. Subsequent 3D classification without alignment enabled separation of tRNA–mRNA bound ribosomes from vacant particles, resulting in a subset of 78,814 particles that improved the reconstruction to 3.0 Å resolution. Further refinement through CTF correction and particle polishing enhanced the map to 2.86 Å. Finally, multi-body refinement was applied, yielding a high-resolution structure at 2.41 Å for the full ribosome, with local resolutions of 2.44 Å for the LSU and 2.70 Å for the SSU (Supplementary Figure 11 and Supplementary Table 1).

Model building and refinement

rRNA and rProteins structures were built by combining template-guided and de novo model building in COOT [39]. The coordinates of PDBID 4UG0 [40] and PDBID 8G6J [41] were used as a reference template for modeling. For atomic model refinement, we used a composite map obtained by aligning and combining the locally refined 40S and 60S maps into a polished 80S map. Model refinement was performed against the composite map using an iterative approach, including real-space refinement and geometry regularization in COOT, followed by real-space refinement using PHENIX [42]. The final model was validated using MolProbity [43]. Sequence alignments were done using Jalview [44]. Figures were generated using UCSF Chimera [45] and UCSF ChimeraX [46, 47].

Puromycin labelling

Cells were plated in a 10cm dish and puromycin (10 µg/ml) was added for 2.5, 5, and 10 min. The cells were lysed using RLB buffer (Promega) and lysates were analyzed by Western blotting.

Western blot and antibodies.

Lysates were subjected to SDS–PAGE followed by western blot using the following antibodies: anti-RPS26 (HPA043961, Atlas Antibodies), anti-RPS3 (AAS09637C, Antibody verify), anti-

puromycin (MABE343, Millipore) and anti-tubulin (AB7291, Abcam). The antibody anti-RPS26 C-terminus was generated in our lab.

Library preparation for Ribo-seq, TIS-seq, and TCP-seq

Ribo-seq and TIS-seq protocols were adapted from Ingolia et al [16]. For the Ribo-seq, three biological replicates of HEK293 WT and Rps26dC cells were grown to 90% confluency on standard conditions and treated with CHX for 5 minutes at 37 degrees. For the TIS-seq, three biological replicates were treated with CHX for 5 minutes and Harringtonine for 2 minutes at 37^{o}C. After removing the media with aspiration, cells were washed with cold PBS and then lysed with fresh lysis buffer (100mM KCl, 20mM Tris-HCl pH 8, 1.5mM MgCl2, 1.5% (v/v) NP-40, 2mM DTT, Protease Inhibitor 1:100) in slow agitation at 4 degrees. Lysates were clarified by centrifugation at 20,000g for 10 minutes. 10% of the lysate was kept and stored apart for the extraction of the total mRNA. The library of total mRNA of Ribo-seq and TIS-seq was prepared with the TruSeq Stranded mRNA Library Prep (Illumina, 20020594) according to manufacturer's protocol.

The TCP-seq protocol was adapted from Weiss et al. Two biological replicates of HEK293 WT and Rps26dC cells grown to 90% confluency were treated with 0.3% of formaldehyde for 5 minutes on ice at slow shaking. The fixation was then interrupted by adding 37.5mM glycine for 5 minutes on ice with slow shaking. After removing the media with aspiration, cells were washed with cold PBS and then lysed with fresh lysis buffer (100mM KCl, 20mM Tris-HCl pH 8, 1.5mM MgCl2, 1.5% (v/v) NP-40, 2mM DTT, Protease Inhibitor 1:100) in slow agitation at 4 degrees. Lysates were clarified by centrifugation at 20,000g for 10 minutes. Digestion of the RNA was performed with the addition of 0.0125U RNAse I per ug of RNA to the lysate for 30 minutes at RT. Digestion was stopped by adding Super RNase inhibitor (ThermoFischer). Lysates were loaded onto a 5-45% sucrose gradient (100mM KCl, 20mM HEPES pH 7, 5mM MgCl2, 2 mM DTT) and centrifuged at 35,000 rpm for 3h at 4 degrees. RNA levels per gradient have been analyzed by TRIAX flowcell while fractionated in 300ul fractions. The TCP-seq libraries were sequenced on Illumina NextSeq High Output - 75 cycles.

Mapping and data analysis

For the Ribo-seq and TIS-seq data analysis, the different samples were demultiplexed according to the given index, and the adaptor sequence was removed as described [16]. rRNA was removed

by aligning sequences to rRNA database from RNAcentral [48] using bowtie2. Next, sequences were filtered to include only 28-32nt long sequences using cutadapt. Sequences were aligned to human transcriptome using STAR aligner (with parameters: –outFilterMultimaoNmax 1) while transcriptome data hg38 filtered by MANEv108 (UCSC) was selected for the alignment. The number of reads per sample (CPM) was calculated for normalization. For quality control, we checked if similar samples clustered together. Metagene plot was prepared using ribo-waltz R-package and TE for each gene was calculated by dividing each gene reads with its total RNA reads [49]. A gene was defined as downregulated if relative to WT log2(TE)< -0.6 and upregulated if log2(TE) > 0.6 for both samples of the same treatment. 5'UTR length and the frequency of nucleotides surrounding the main ORF AUG were determined using R Bioconductor and logos packages. The presence of uORFs in each gene's 5'UTR was determined from the TIS-seq data as previously described [50]. This allowed the identification of initiation sites (MACS callpeak, -q 0.01) and extraction of all possible start locations for uORFs and using MACS2. We determined if the initiation site has an in-frame stop codon before the main ORF and, therefore, defined it as uORF. For the total RNA data analysis, we used the UTAP transcriptome analysis pipeline [49]. The Raw reads were trimmed using cutadapt. Reads were mapped to the human genome (hg38) using STAR with the parameters –alignEndsType EndToEnd, –outFilterMismatchNoverLmax 0.05. The pipeline quantifies the 3’ of Gencode annotated genes (1,000 bases upstream of the 3’ end and 100 bases downstream). UMI counting was done after marking duplicates (in-house script) using HTSeq- count in union mode. The reads with unique mapping were used for the analysis, and a minimum of 5 reads in at least one sample was set.

For the TCP-seq, adapters were trimmed from with cutadapt[51] (parameters: -a CTGTAGGCACCATCAAT -m 16) and reads were filtered by quality with TRIMMOMATIC[52] (parameters: MINLEN:16 TRAILING:15 SLIDINGWINDOW:5:15). Reads were filtered out by successive mapping to rRNAs (UCSC) and to tRNAs (GtrRNA database) with bowtie[53] and to lncRNAs (Ensembl) with HISAT2.[54] Unmapped reads were finally aligned to the human MANE transcriptome (Ensemble release 108) with HISAT2 using default parameters. Finally, only primary alignments were kept for the analysis. Subsequently, the data was analysed as recently described [15].

To identify translated upstream open reading frames (uORFs), we mapped translation initiation sites (TISs) genome-wide using MACS2 peak calling on HAR and cycloheximide (CHX)–treated ribosome profiling libraries. Peaks were called with MACS2 using the parameters --nomodel, --extsize 1, and -q 0.01, and imported as genomic ranges. Peaks overlapping annotated 5'UTRs and supported by >10 CPM were retained as high-confidence uORF start sites. For each start site, the corresponding uORF was defined by extending to the first in-frame stop codon. To focus on biologically relevant uORFs, we designated as *active uORFs* only those originating from transcripts present in the CDS-level translation efficiency (TE) dataset, ensuring that the main ORF of the transcript is actively translated and TE can be reliably quantified for downstream analyses

Mass spectrometry analysis

The 40S, 43S and 48S were isolated and collected from two biological replicates of HEK293 WT and RPS26dC cells by sucrose gradient. The pulled fractions were lysed and digested with trypsin using the S-trap method. The resulting peptides were analyzed using nanoflow liquid chromatography (nanoAcquity) coupled to high resolution, high mass accuracy mass spectrometry (Q Exactive HF). Each sample was analyzed on the instrument separately in a random order in discovery mode.

Raw data was processed with MetaMorpheus version 0.0.320. The data was searched against the human proteome database appended with common lab protein contaminants and the default modifications. Quantification was performed using the embedded FlashLFQ and protein inference algorithms.

Polysome profiling

WT and RPS26dC at 90% of confluency were incubated with 100 µg/ml cycloheximide (CHX, Sigma) for 5 min and then washed twice with cold PBS plus 100 µg/ml CHX. Cells were then scraped in 500 µl of lysis buffer (100mM KCl, 20mM Tris-HCl pH 8, 1.5mM MgCl2, 1.5% (v/v) NP-40, 2mM DTT, Protease Inhibitor 1:100, 100 ug/ml CHX) and subsequentially incubated in a 4^{o}C shaker for 30 min. The lyzed samples were centrifuged at 12 000 × g at 4°C for 5 min. The cleared lysates were loaded onto a 5–45% sucrose gradient and centrifuged at 35 000 rpm in an SW41 rotor for 3h at 4°C or 10-50% sucrose gradient and centrifuged at 39 000 rpm in an SW41 rotor

for 1:45h at 4°C. Gradients were fractionated and the optical density at 254 nm was continuously recorded using the ISCO absorbance detector UA-6.

Generation of reporter gene plasmids

The CTR-K (*Firefly* luciferase construct) and *Renilla* luciferase plasmids were previously described [55]. The CTR-RI and CTR-LS plasmids were previously described [56]. All the following constructs have been made through restriction-free cloning using the primers listed in Supplementary Table 2. To generate the CTR-W construct, nucleotides around the starting AUG were mutated to generate a weak AUG context using the CTR-K construct as template along with primers #1, 2 (here and on, see Supplementary Table 2 for primer sequences). To generate the H2B-5'UTR construct, the 5'UTR and the AUG context of H2BC4 were inserted using the CTR-K as template along with primers #3 and 4. To generate the TISU-LIKE construct, its sequence was inserted using the H2B-5'UTR construct as template along with primers #5 and 6. To generate the H2B-3'UTR construct, the histone 3'UTR was inserted using the CTR-K construct as template along with primers #7 and 8. To generate the H3-5'UTR construct, the 5'UTR and the AUG context of H3C12 were inserted using the CTR-K construct as template along with primers #9 and 10. To generate the H2B-16nt and H2B-10nt constructs, the 5'UTR of the H2B-5'UTR construct was shortened up to 16 nt or 10 nt, using the H2B-5'UTR construct as template along with primers #11,12 and 13, 14, respectively. To generate the H3-16nt and H3-10nt constructs, the 5'UTR of H3-5'UTR construct was shortened up to 16 nt or 10 nt, using the H3-5'UTR construct as template along with primers #15, 16 and 17, 18, respectively. To generate the Mut +5, the C in position +5 was mutated into an A using the H2B-5'UTR construct as template along with primers #19 and 20. To generate the Mut -5/-6 construct, the T in positions -5 and -6 were mutated into G using the H2B-5'UTR construct as template along with primers #21 and 22. To generate the Mut -9 to -16 construct, the T(s) from position -9 to -16 were mutated into G using the H2B-5'UTR construct as template along with primers #23 and 24. To generate the Mut -5/-6, -9 to -16 construct, the T in positions -5, -6 and from position -9 to -16 were mutated into G using the H2B-5'UTR construct as template along with primers #25 and 26. To generate the H2B-LS and H3-LS and TISU-LIKE-LS constructs, a second AUG in-frame with the FLuc but out of frame with the AUG of the respective 5'UTR was added using the respective 5'UTR constructs as templates along with primers #27-32. To generate the

TISU-G and the TISU-C constructs, the TISU element with a G or C in position -4 was inserted using the H2B-5'UTR construct as template along with primers #33, 34 and 37, 38 respectively. To generate the TISU-G-LS and TISU-C-LS constructs, a second AUG in frame with the FLuc reporter but out of frame with the first AUG driven by the TISU-G or TISU-C context was added using the H2B-LS construct as template along with primers #35, 36 and 39, 40, respectively. To generate the TISU-C-6AA construct, a second AUG driven by Kozak context was inserted exactly 18 nucleotides after the first AUG, making the second AUG in frame with the first. The insertion was made using the TISU-C construct as template along with primers #41, 42. The TISU-C-6AA-LS, TISU-C-6AA, TISU-LIKE-3AA, TISU-LIKE-3AA-LS, TISU-LIKE-6AA and TISU-LIKE-6AA-LS were similarly generated using primers #43-52.

In vitro transcription and mRNA capping

For the synthesis of the H2B-5UTR-Firefly mRNA and the control Renilla luciferase, we generated linearized fragments by PCR with the addition of the T7 promoter in the forward primers. The linearized products were purified with ethanol precipitation and used as a template for in vitro transcription and DNase treatment using T7 RiboMAX™ Express Large Scale RNA Production System (Promega). The mRNAs were purified through Lithium Chloride precipitation. Then, 10 ug of mRNA was subsequently capped using the Vaccinia Capping System (New England Biolabs), followed by precipitation using lithium chloride.

Cell transfection and reporter gene assays

DNA transfections were done by the calcium phosphate method (2x HEPES buffer saline, 554Bf). Lipofectamine 2000 (11668027, Invitrogen™) was used for the RNA transfection. For the plasmid-based reporter assays, cells were plated in 24-well plates, 80,000 cells per well for WT cells and 100,000 cells per well for Rps26dC cells. 24 hours later, cells were co-transfected with the indicated Firefly luciferase constructs along with a Renilla luciferase that served as a normalizer of transfection efficiency. Cells were harvested 24h after transfection, and luminescence activities were determined. For RNA transfection, WT and Rps26dC cells at 80% confluency were plated in a 24-well plate. 500ng of H2B-5'UTR and 150ng of Renilla (normalizer for transfection efficiency) mRNAs were transfected into each well. 2 hours after the transfection, the medium was changed

with fresh medium, and 6 hours after the transfection, cells were harvested, lysed, and Firefly and Renilla luminescence were read.

Statistical analysis.

For the TCP-seq analysis, Welch test was conducted between two groups using R version 4.4. Student's t-test has been performed to assign statistical significance to luminescence experiments.

For differential expression analysis of ribosome profiling (Ribo-seq) and matched RNA-seq data, DESeq2 (v1.40.2) was used. A likelihood ratio test (LRT) was performed to compare the full model (~ library + treatment + condition) against a reduced model (~ library + treatment), allowing identification of transcripts with treatment-specific translational regulation. Significantly differentially expressed genes were defined using an adjusted p-value (FDR) threshold of < 0.05 and an absolute log2 fold change > 0.6 (corresponding to a fold change > 1.5). Results were extracted using the results() function in DESeq2 and downstream filtering and visualization were performed in R using tidyverse tools.

Data availability

The cryo-EM density maps of the 80S ribosome complexes have been deposited in the Electron Microscopy Data Bank (EMDB) under accession numbers EMD-54265 (WT-Kozak), EMD-54266 (WT-TISU), EMD-54267 (RPS26dC-Kozak), EMD-54268 (RPS26dC-TISU), and EMD-54269 (WT-H2B). The corresponding atomic coordinates have been deposited in the Protein Data Bank (PDB) under accession codes 9RU7 (WT-Kozak), 9RU8 (WT-TISU), 9RU9 (RPS26dC-Kozak), 9RUA (RPS26dC-TISU), and 9RUC (WT-H2B).

TCP-seq, Ribo-seq, TiS-seq, and RNA-seq datasets have been deposited in the NCBI Gene Expression Omnibus (GEO) under Series accession numbers GSE294217, GSE301926 , and GSE301928.

References

1. Farrar JE*, et al.* Ribosomal protein gene deletions in Diamond-Blackfan anemia. *Blood* **118**, 6943-6951 (2011).

2. Bolze A*, et al.* Ribosomal protein SA haploinsufficiency in humans with isolated congenital asplenia. *Science* **340**, 976-978 (2013).

3. Ebert BL*, et al.* Identification of RPS14 as a 5q- syndrome gene by RNA interference screen. *Nature* **451**, 335-339 (2008).

4. Burwick N, Shimamura A, Liu JM. Non-Diamond Blackfan anemia disorders of ribosome function: Shwachman Diamond syndrome and 5q- syndrome. *Semin Hematol* **48**, 136-143 (2011).

5. Gerst JE. Pimp My Ribosome: Ribosomal Protein Paralogs Specify Translational Control. *Trends Genet* **34**, 832-845 (2018).

6. Genuth NR, Barna M. The Discovery of Ribosome Heterogeneity and Its Implications for Gene Regulation and Organismal Life. *Mol Cell* **71**, 364-374 (2018).

7. Sulima SO, Dinman JD. The Expanding Riboverse. *Cells* **8**, (2019).

8. Ferretti MB, Karbstein K. Does functional specialization of ribosomes really exist? *RNA* **25**, 521-538 (2019).

9. Mauro VP, Edelman GM. The ribosome filter redux. *Cell cycle* **6**, 2246-2251 (2007).

10. Gay DM, Lund AH, Jansson MD. Translational control through ribosome heterogeneity and functional specialization. *Trends in biochemical sciences* **47**, 66-81 (2022).

11. Haimov O*, et al.* Efficient and Accurate Translation Initiation Directed by TISU Involves RPS3 and RPS10e Binding and Differential Eukaryotic Initiation Factor 1A Regulation. *Mol Cell Biol* **37**, e00150-00117 (2017).

12. Pisarev AV, Kolupaeva VG, Yusupov MM, Hellen CU, Pestova TV. Ribosomal position and contacts of mRNA in eukaryotic translation initiation complexes. *The EMBO journal* **27**, 1609-1621 (2008).

13. Havkin-Solomon T*, et al.* Translation regulation of specific mRNAs by RPS26 C-terminal RNA-binding tail integrates energy metabolism and AMPK-mTOR signaling. *Nucleic acids research* **51**, 4415-4428 (2023).

14. Havkin-Solomon T, Itzhaki E, Joffe N, Reuven N, Shaul Y, Dikstein R. Selective translational control of cellular and viral mRNAs by RPS3 mRNA binding. *Nucleic acids research* **51**, 4208-4222 (2023).

15. Weiss B, Dikstein R. Unraveling the landscapes and regulation of scanning, leaky scanning, and 48S initiation complex conformations. *Cell reports* **43**, 114126 (2024).

16. Ingolia NT, Brar GA, Rouskin S, McGeachy AM, Weissman JS. The ribosome profiling strategy for monitoring translation in vivo by deep sequencing of ribosome-protected mRNA fragments. *Nature protocols* **7**, 1534-1550 (2012).

17. Ge SX, Jung D, Yao R. ShinyGO: a graphical gene-set enrichment tool for animals and plants. *Bioinformatics* **36**, 2628-2629 (2020).

18. Marzluff WF, Wagner EJ, Duronio RJ. Metabolism and regulation of canonical histone mRNAs: life without a poly(A) tail. *Nature reviews Genetics* **9**, 843-854 (2008).

19. Hayek H*, et al.* eIF3 interacts with histone H4 messenger RNA to regulate its translation. *The Journal of biological chemistry* **296**, 100578 (2021).

20. Haimov O, Sinvani H, Dikstein R. Cap-dependent, scanning-free translation initiation mechanisms. *Biochim Biophys Acta* **1849**, 1313-1318 (2015).

21. Jia L, Qian SB. Therapeutic mRNA Engineering from Head to Tail. *Acc Chem Res* **54**, 4272-4282 (2021).

22. Youssef M, Hitti C, Puppin Chaves Fulber J, Kamen AA. Enabling mRNA Therapeutics: Current Landscape and Challenges in Manufacturing. *Biomolecules* **13**, (2023).

23. Elfakess R, Dikstein R. A translation initiation element specific to mRNAs with very short 5'UTR that also regulates transcription. *PloS one* **3**, e3094 (2008).

24. Elfakess R, Sinvani H, Haimov O, Svitkin Y, Sonenberg N, Dikstein R. Unique translation initiation of mRNAs-containing TISU element. *Nucleic acids research* **39**, 7598-7609 (2011).

25. Svitkin YV*, et al.* The requirement for eukaryotic initiation factor 4A (elF4A) in translation is in direct proportion to the degree of mRNA 5' secondary structure. *Rna* **7**, 382-394 (2001).

26. Sen ND, Gupta N, S KA, Preiss T, Lorsch JR, Hinnebusch AG. Functional interplay between DEAD-box RNA helicases Ded1 and Dbp1 in preinitiation complex attachment and scanning on structured mRNAs in vivo. *Nucleic acids research* **47**, 8785-8806 (2019).

27. Jaeger S, Barends S, Giege R, Eriani G, Martin F. Expression of metazoan replication-dependent histone genes. *Biochimie* **87**, 827-834 (2005).

28. Martin F, Barends S, Jaeger S, Schaeffer L, Prongidi-Fix L, Eriani G. Cap-assisted internal initiation of translation of histone H4. *Mol Cell* **41**, 197-209 (2011).

29. Dominski Z, Marzluff WF. Formation of the 3' end of histone mRNA: getting closer to the end. *Gene* **396**, 373-390 (2007).

30. Kwan T, Thompson SR. Noncanonical Translation Initiation in Eukaryotes. *Cold Spring Harbor perspectives in biology* **11**, (2019).

31. Ferretti MB, Ghalei H, Ward EA, Potts EL, Karbstein K. Rps26 directs mRNA-specific translation by recognition of Kozak sequence elements. *Nature structural & molecular biology* **24**, 700-707 (2017).

32. Sinvani H*, et al.* Translational tolerance of mitochondrial genes to metabolic energy stress involves TISU and eIF1-eIF4GI cooperation in start codon selection. *Cell metabolism* **21**, 479-492 (2015).

33. Petrychenko V, Yi SH, Liedtke D, Peng BZ, Rodnina MV, Fischer N. Structural basis for translational control by the human 48S initiation complex. *Nature structural & molecular biology*, (2024).

34. Burt A*, et al.* An image processing pipeline for electron cryo-tomography in RELION-5. *FEBS open bio*, (2024).

35. Zheng SQ, Palovcak E, Armache J-P, Verba KA, Cheng Y, Agard DA. MotionCor2: anisotropic correction of beam-induced motion for improved cryo-electron microscopy. *Nat Methods* **14**, 331-332 (2017).

36. Mindell JA, Grigorieff N. Accurate determination of local defocus and specimen tilt in electron microscopy. *Journal of structural biology* **142**, 334-347 (2003).

37. Kimanius D, Dong L, Sharov G, Nakane T, Scheres SA-O. New tools for automated cryo-EM single-particle analysis in RELION-4.0. *Biochem J* **478(24)**, 4169-4185 (2021).

38. Nakane T, Kimanius D, Lindahl E, Scheres SH. Characterisation of molecular motions in cryo-EM single-particle data by multi-body refinement in RELION. *eLife* **7**, (2018).

39. Emsley P, Lohkamp B, Scott WG, Cowtan K. Features and development of Coot. *Acta Crystallographica Section D: Biological Crystallography* **66**, 486-501 (2010).

40. Khatter H, Myasnikov AG, Natchiar SK, Klaholz BP. Structure of the human 80S ribosome. *Nature* **520**, 640-645 (2015).

41. Holm M*, et al.* mRNA decoding in human is kinetically and structurally distinct from bacteria. *Nature* **617**, 200-207 (2023).

42. Afonine PV*, et al.* Real-space refinement in PHENIX for cryo-EM and crystallography. *Acta crystallographica Section D, Structural biology* **74**, 531-544 (2018).

43. Williams CJ*, et al.* MolProbity: More and better reference data for improved all-atom structure validation. *Protein Sci* **27**, 293-315 (2018).

44. Waterhouse AM, Procter JB, Martin DMA, Clamp M, Barton GJ. Jalview Version 2-A multiple sequence alignment editor and analysis workbench. *Bioinformatics* **25**, 1189-1191 (2009).

45. Pettersen EF*, et al.* UCSF Chimera - A visualization system for exploratory research and analysis. *Journal of computational chemistry* **25**, 1605-1612 (2004).

46. Goddard TD*, et al.* UCSF ChimeraX: Meeting modern challenges in visualization and analysis. *Protein Sci* **27**, 14-25 (2018).

47. Pettersen EF*, et al.* UCSF ChimeraX: Structure visualization for researchers, educators, and developers. *Protein Sci* **30**, 70-82 (2021).

48. The RC*, et al.* RNAcentral: a comprehensive database of non-coding RNA sequences. *Nucleic acids research* **45**, D128-D134 (2017).

49. Kohen R*, et al.* UTAP: User-friendly Transcriptome Analysis Pipeline. *BMC bioinformatics* **20**, 154 (2019).

50. Sehrawat U*, et al.* Inhibitors of eIF4G1-eIF1 uncover its regulatory role of ER/UPR stress-response genes independent of eIF2-alpha-phosphorylation. *Proceedings of the National Academy of Sciences* **119**, e2120339119 (2022).

51. Martin M. Cutadapt removes adapter sequences from high-throughput sequencing reads. *2011* **17**, 3 (2011).

52. Bolger AM, Lohse M, Usadel B. Trimmomatic: a flexible trimmer for Illumina sequence data. *Bioinformatics* **30**, 2114-2120 (2014).

53. Langmead B, Trapnell C, Pop M, Salzberg SL. Ultrafast and memory-efficient alignment of short DNA sequences to the human genome. *Genome Biology* **10**, R25 (2009).

54. Kim D, Langmead B, Salzberg SL. HISAT: a fast spliced aligner with low memory requirements. *Nat Methods* **12**, 357-360 (2015).

55. Sehrawat U, Koning F, Ashkenazi S, Stelzer G, Leshkowitz D, Dikstein R. Cancer-Associated Eukaryotic Translation Initiation Factor 1A Mutants Impair Rps3 and Rps10 Binding and Enhance Scanning of Cell Cycle Genes. *Mol Cell Biol* **39**, e00441-00418 (2019).

56. Hayat D*, et al.* Inhibitors of eIF1A-ribosome interaction unveil uORF-dependent regulation of translation initiation and antitumor and antiviral effects. *The EMBO journal*, (2025).

Acknowledgments

We thank the G-INCPM deep sequencing team of the Weizmann Institute for the RNA-seq. This work was supported by the Israel Science Foundation (#1199/22), the Kimmelman Center for Macromolecular Assemblies, and by Weizmann Institute internal grants from the Estate of Manfred and Margaret Tannen and Joel and Mady Dukler Fund for Cancer Research. R.D. is the incumbent of the Ruth and Leonard Simon Chair of Cancer Research.

Author Contributions

D.F. designed the study, performed experiments, analyzed the data, and wrote the paper; D.G.H. designed the study, performed experiments, analyzed the data, and wrote the paper; B.W. analyzed the TCP-seq data; A.O analyzed the Ribo-seq data; T.H.S. performed an experiment; I.M.R performed an experiment; A.B. designed the study, performed experiments, analyzed the data, and wrote the paper; A.Y. designed the study, analyzed the data, and wrote the paper; R.D. conceived and designed the study, analyzed the data, supervised the project and wrote the paper.

Competing Interests Statement

The authors declare that they have no conflict of interest associated with this study.

Figures legends

Figure 1. **Structural comparison of the human RPS26/eS26-mRNA binding in WT vs. RPS26dC mutant ribosome. A.** mRNA sequences of Kozak and TISU mRNA **B.** WT RPS26/eS26 is shown in pink is superposed on the cryo-EM map, shown in grey (left). RPS26dC mutant eS26 is shown in blue and superposed on the cryo-EM map, shown in grey (Middle). An overlay of WT RPS26/eS26 (pink) and RPS26dC (blue) is shown in the right. The map contour level is 1.9 σ **C.** Zoom into the structure of WT (light pink) ribosomes with Kozak mRNA (gold), showing the RPS26/eS26 and the mRNA and P-site tRNA in the ribosome complex structure. **D.** The interactions of the RPS26/eS26 C-terminus with the backbone of Kozak mRNA (gold) in the structure of WT (pink) ribosome, highlight the stabilizing contact between the C-terminal tails of ribosomal protein RPS26/eS26 and the Kozak mRNA backbone. **E.** Specific interaction between the RPS26/eS26-H80 C-terminus and -5 and -6 nucleotides of Kozak mRNA. **F.** Changes in mRNA stability and ribosome-mRNA interactions within the mutant ribosome complex structure is shown by zooming into the structure of RPS26dC (light blue) mutant ribosomes with Kozak mRNA (gold). **G.** The differential stability of TISU mRNA compared to Kozak mRNA is illustrated by zooming into the structure of WT (pink) ribosomes with TISU mRNA (red). **H.** Altered ribosome-mRNA interaction in the mutant ribosomes is demonstrated by zooming into the structure of RPS26dC (blue) mutant ribosomes with TISU mRNA (red). Throughout, P-site tRNA is colored green. The map contour level is 2.0 σ. **I.** The interaction of RPS26/eS26-H80 with nucleotides of TISU mRNA (red) in WT (pink) ribosomes. **J.** Loss of interaction of the RPS26/eS26-H80 with nucleotides of TISU mRNA (red) in RPS26dC mutant.

Figure 2: Translation initiation and elongation defects in RPS26/eS26 mRNA binding mutant cells. A. WT and RPS26dC cells were treated with puromycin (10 µg/ml) for 2.5, 5 and 10 minutes, after which cells were lysed and analyzed by western blot using an anti-puromycin antibody and anti-Tubulin antibody that serves as a loading control. The graph on the right represents the mean±SEM chemiluminescence signal intensity of puromycin labeling normalized to Tubulin (N=3, N represents the number of biological replicates). The asterisks denote statistically significant differences (*P < 0.05, **P < 0.01) according to Student's t-test (unpaired, two-tailed). The difference between WT 5min and RPS26dC 5 min is statistically significant (p = 0.01641). The difference between WT 10min and RPS26dC 10 min is statistically significant (p = 0.00099). **B.** WT and RPS26dC HEK293T cells were subjected to TCP-seq library preparation, sequencing, and mapping. Mapped protected RNA footprints were subjected to metagene analysis of the normalized 40S footprints (FP) counts on the 5'UTR (left) and CDS (right) regions. WT is represented in black and RPS26dC in red. **C.** The relative number of reads based on the length is represented. WT and RPS26dC are in black and red, respectively **D.** Plots of the normalized 5'-end read count around the start codon. WT is represented in black and RPS26dC in red. **E.** Plots of the normalized 3'-end read counts around the start codon. WT is represented in black and RPS26dC in red. **F.** A scheme representing the different populations of reads around the starting codon. The green denotes reads ending at +24, The red reads ending at +1 and the blue are reads spanning -12 to +24. **G.** The AUG context of transcripts with cut in position +/-1 in WT (upper panel) and mutant (lower panel) samples. **H.** Violin Plots of the length distribution of reads that end between +19 and +24/+26. WT is represented in black, RPS26dC is represented in red. The

asterisk indicates statistically significant differences (****P<0.001) according to Welsch Student's T-Test (unpaired, two-tailed) (p = 2.22e-16). **I.** A scheme showing the slow scanning and elongating 40S and 80S ribosomes in WT (left) and RPS26dC cells according to the analysis presented in sections B and E.

Figure 3: RPS26dC mutant cells exhibit reduced size of ribosome occupancy during initiation and elongation. WT and RPS26dC mutant cells were subjected to CHX or CHX plus Harringtonine (HAR) treatments for Ribo-seq and TIS-seq, respectively, as detailed in Materials and Methods. In parallel, the same samples were also subjected to RNA-seq for total mRNA level measurements. **A.** Metagene analysis of the Ribo-seq (left) and TIS-seq (right). WT is represented in black and RPS26dC in red. **B.** Read-length distribution of ribosome-protected fragments in CHX-treated samples. Bars represent the mean normalized percentage of reads per read length (25–32 nt) across biological replicates. Error bars indicate ± SEM. Black dots represent individual biological replicates (N=3). WT control group is in gray; RPS26ΔC is in magenta. **C.** Metagene analyses of the Ribo-seq libraries based on the read length (starting from the left: 27nt, 28nt and 29nt long). WT is represented in black and RPS26dC in red. **D.** A histogram representing the normalized count based on the transcripts with predominant TIS-seq read length (>50%). WT is represented in black and RPS26dC in red. **E.** A table showing the number of downregulated or upregulated genes based on the ration of normalized CDS Ribo-seq reads to total RNA-seq reads of each gene, in RPS26dC compared to WT cells treated with CHX. 1.7-fold change difference has been used as the threshold. **F.** Motif sequence around the start codon of transcripts that are unchanged (left), downregulated (center), and upregulated (right) in RPS26dC compared to WT cells. **G-H.** A zoom-in of the Cryo-EM visualization of the stacking interaction of the 18S G1207 with the -1 position of Kozak (gold) and TISU (red) mRNAs in WT cells. **(I)** Visualization of the shifted interaction of the 18S G1207 from the -1 position to the -2 nucleotide of Kozak mRNA in RPS26dC mutant cells.

Figure 4: Characterization of histone 5'UTR translational enhancer as a primary target of RPS26/eS26 C-terminal mRNA binding. A. Analysis of biological function and gene categories of RPS26dC translationally downregulated mRNAs using the ShinyGo tool. The arrows indicate the two most affected categories. **B.** Boxplot comparing 5'UTR length between histone transcripts and all other cellular transcripts. The centre line indicates the median. The bounds of the box represent the 25th and 75th percentiles (interquartile range, IQR). Whiskers extend to the minimum and maximum values (or, if applicable, to 1.5 × IQR from the quartiles). **C.** Motif sequence around the start codon of histone transcripts. **D.** Read-length distributions are shown for all transcripts and histone transcripts. Bars represent the mean normalized percentage of reads per read length (25–32 nt) across biological replicates. Error bars indicate ± SEM. Black dots represent individual biological replicates (N=3). WT control is in gray; RPS26ΔC is in magenta. **E.** Plots of the normalized 3'end read count of downregulated histone transcripts around the start codon. WT is represented in black and RPS26dC in red. **F.** The firefly luciferase (FF) constructs shown schematically in the left panel were co-transfected into HEK293T cells WT (black) and RPS26dC (red), together with Renilla luciferase (RL), which serves as a normalizing control. Cells were harvested 24 h after transfection, and FF and RL levels were measured (CTR-K WT N=4, CTR-K dC N=4, CTR-W WT N=3, CTR-W dC N=3, H2B-5'UTR WT N=23, H2B-5'UTR dC N=23, TISU-LIKE WT N=12, TISU-LIKE dC N=4, H3-5'UTR WT N=5, H3-5'UTR dC N=5, H2B-3'UTR WT N=3, H2B-3'UTR

dC N=3. N represents the number of biological replicates). An asterisk denotes a statistically significant difference (**P < 0.01, ***P<0.005) according to Student's t-test (unpaired, two-tailed). These differences are statistically significant: CTR-K WT and CTR-K dC p = 0.008587796); CTR-K WT and H2B-5'UTR WT p = 1.64597E-06; CTR-K WT and H2B-3'UTR p = 1.07656E-05; H2B-5'UTR WT and H2B-5'UTR dC p = 3.7621E-12; TISU-LIKE WT and TISU-LIKE dC p = 0.000410087; H2B-3'UTR WT and H2B-3'UTR dC p = 0.008625152; H3-5'UTR WT and H3-5'UTR dC p = 0.006986665. Data are presented as mean values +/- SEM. **G.** H2B-5'UTR and control Renilla construct were transcribed and capped in vitro. WT and RPS26dC cells were transfected with the capped mRNAs. 6h after transfection, cells were harvested, and FF and RL activities were measured (the number of biological replicates N=6). An asterisk denotes a statistically significant difference (****P < 0.001) according to Student's t-test (unpaired, two-tailed). The difference between WT and dC is statistically significant (p = 0.0001). Data are presented as mean values +/- SEM. **H.** The H2B-16nt and H2B-10nt reporter genes were co-transfected into WT (black) and RPS26dC (red) cells together with the RL control plasmid. Cells were harvested 24 h after transfection and luciferase levels were measured (the number of biological replicates N=8). An asterisk denotes a statistically significant difference (***P < 0.005) according to Student's t-test (unpaired, one-tailed). The difference between H2B-10 WT and H2B-16 WT is statistically significant (p = 0.0002). Data are presented as mean values +/- SEM. **I.** H3-16nt and H3-10nt reporter genes were co-transfected into WT (black) and RPS26dC (red) cells together with the RL control plasmid. Cells were harvested 24 h after transfection and luciferase levels were measured (the number of biological replicates N=4). An asterisk denotes a statistically significant difference (**P < 0.01) according to Student's t-test (unpaired, one-tailed). The difference between H3-10 WT and H3-16 WT is statistically significant (p = 0.0068). Data are presented as mean values +/- SEM. **J.** The left panel presents a scheme of the various mutations in H2B 5'UTR, and the AUG context is shown. In the middle panel, the WT and mutant H2B-5'UTR constructs were co-transfected into WT (black) and RPS26dC (red) cells together with the RL control plasmid. Cells were harvested 24 h after transfection and luciferase levels were measured (H2B-5'UTR WT N=23, H2B-5'UTR dC N=23, Mut +5 WT N=3, Mut +5 dC N=3, Mut -5-6 WT N=6, Mut -5-6 dC N=6, Mut -9-16 WT N=6, Mut -9-16 dC N=6, Mut -5-6-9/-16 WT N=3, Mut -5-6-9/-16 dC N=3. N represents the number of biological replicates). The relative activities in the WT and RPS26dC cells are presented in black and red, respectively. An asterisk denotes a statistically significant difference (*P < 0.05, ***P < 0.005) according to Student's t-test (unpaired, one-tailed). The difference between H2B-5'UTR WT and Mut -9-16 WT is statistically significant (p = 0.0001), and also that between H2B-5'UTR WT and Mut -5-6-9/-16 WT (p = 0.0143). Data are presented as mean values +/- SEM. The right panel shows a comparison of the inhibitory effect of the -9/-16 mutation on translation (Mut -9/16 signal/H2B-5'UTR signal) in WT and RPS26dC cells (the number of biological replicates N=7). WT is represented in black and RPS26dC in red. An asterisk denotes a statistically significant difference (*P < 0.05) according to Student's t-test (paired, one-tailed). The difference between WT and dC is statistically significant (p = 0.05). Data are presented as mean values +/- SEM.

Figure 5: **Structural insights into RPS26/eS26 interactions with H2B mRNA. A.** Nucleotide sequence of the H2B mRNA used for structural studies. **B.** Close-up view of the cryo-EM structure of the WT ribosome (shown in light pink) bound to H2B mRNA (purple), with clear visualization

of RPS26/eS26 and the P-site tRNA within the mRNA–tRNA–ribosome complex. **C.** Detailed depiction of the specific stacking interaction between the H80 in RPS26/eS26 and the -4 nucleotide of H2B mRNA. **D.** Zoomed-in view of the base-stacking interaction between the conserved G1207 residue of 18S rRNA (salmon) and the -1 nucleotide of H2B mRNA, which remains intact in the WT ribosome-H2B complex. **E–G.** Comparative structures showing the positioning of key mRNA exit-channel proteins (uS5, uS14, eS26, and eS28) in ribosome complexes bound to Kozak (E), H2B (F), and TISU (G) mRNAs, illustrating context-dependent remodeling of the mRNA-binding interface. **H.** Distinct conformations of the RPS26/eS26 C-terminal tail depending on the 5'UTR sequence as revealed by structural superimposition of the exit-channel proteins from all three complexes, supporting a model in which RPS26 dynamically adapts conformation in a sequence-specific manner.

Figure 6: A 5'UTR length-dependent effect on leaky scanning and an engineered expression cassette based on H2B-5'UTR. A. Boxplots show 5'UTR lengths for transcripts with significantly increased ("Up LS", n = 159 transcripts) or decreased ("Down LS", n = 244 transcripts) leaky scanning in RPS26ΔC cells compared to WT. Each data point corresponds to one annotated transcript (unit of study); no biological or technical replicates apply to this transcript-level computational analysis. The center line indicates the median; box limits denote the 25th and 75th percentiles (IQR). Whiskers extend to the most extreme values within 1.5 × IQR; values beyond are shown as outliers. Notches indicate the approximate 95% confidence interval of the median. **B.** A scheme of constructs generated to measure the extent of leaky scanning in H2B and H3 5'UTRs is shown at the top. The extent of leaky scanning (H2B-LS/H2B-5'UTR and H3-LS/H3-5'UTR) in WT and RPS26dC mutant cells is shown in the bottom panel (H2B-LS/H2B-5'UTR WT N=5, H2B-LS/H2B-5'UTR dC N=5, H3-LS/H3-5'UTR WT N=4, H3-LS/H3-5'UTR dC N=4. N represents the number of biological replicates). WT is represented in black and RPS26dC in red. An asterisk denotes a statistically significant difference (*P < 0.05) according to Student's t-test (unpaired, two-tailed). The activity of each construct is shown in Supplementary Figure 12A. The difference between H2B-LS/H2B-5'UTR WT and H2B-LS/H2B-5'UTR dC is statistically significant (p = 0.0297). Data are presented as mean values +/- SEM. **C.** The extent of leaky scanning (left) and re-initiation level (right) in WT and RPS26dC mutant cells in long 5'UTR as shown schematically on the top (the number of biological replicates N=3). WT is represented in black and RPS26dC in red. An asterisk denotes a statistically significant difference (**P < 0.01) according to Student's t-test (unpaired, two-tailed). The difference between CTR-LS/CTR-K WT and CTR-LS/CTR-K dC is statistically significant (p = 0.0017). Data are presented as mean values +/- SEM. **D.** Generation of H2B 5'UTR and H2B-5'UTR-LS variant pairs bearing distinct AUG contexts are shown in the upper scheme. These constructs were transfected into WT cells, which were harvested 24 hours later, and luciferase levels were measured (CTR N=3, CTR-LS N=3, H2B5UTR N=28, H2B5UTR-LS N=9, TISU-LIKE N=12, TISU-LIKE-LS N=12, TISU-G N=20, TISU-G-LS N=16, TISU-C N=16, TISU-C-LS N=16. N represents the number of biological replicates). Data are presented as mean values +/- SEM. **E.** Additional H2B 5'UTR and H2B-5'UTR-LS variant pairs engineered to further reduce LS are shown on the top and their activity is presented in the graph below (CTR N=3, CTR-LS N=3, H2B5UTR N=28, H2B5UTR-LS N=9, TISU-C-6AA N=8, TISU-C-6AA-LS N=4, TISU-LIKE 3AA N=4, TISU LIKE 3AA LS N=4, TISU LIKE 6AA N=4, TISU LIKE 6AA LS N=8. N represents the number of biological replicates). Data are presented as mean values +/- SEM. **F.** A summary graph comparing the extent

of LS of the constructs shown in Figure 6D and E, obtained by dividing each LS construct by its respective construct without leaky scanning (CTR N=3, H2B5UTR N=6, TISU-LIKE N=8, TISU-G N=16, TISU-C N=16, TISU-C-6AA N=8, TISU-LIKE 3AA N=4, TISU LIKE 6AA N=4. N represents the number of biological replicates). Data are presented as mean values +/- SEM.

Editorial Summary

The ribosome mRNA channel is central to translation, yet its role in regulatory mechanisms remains unclear. Here the authors, reveal insights into the structural and regulatory landscape of RPS26/eS26 mRNA binding in mammalian cells.

Peer Review Information: *Nature Communications* thanks the anonymous reviewers for their contribution to the peer review of this work. A peer review file is available.

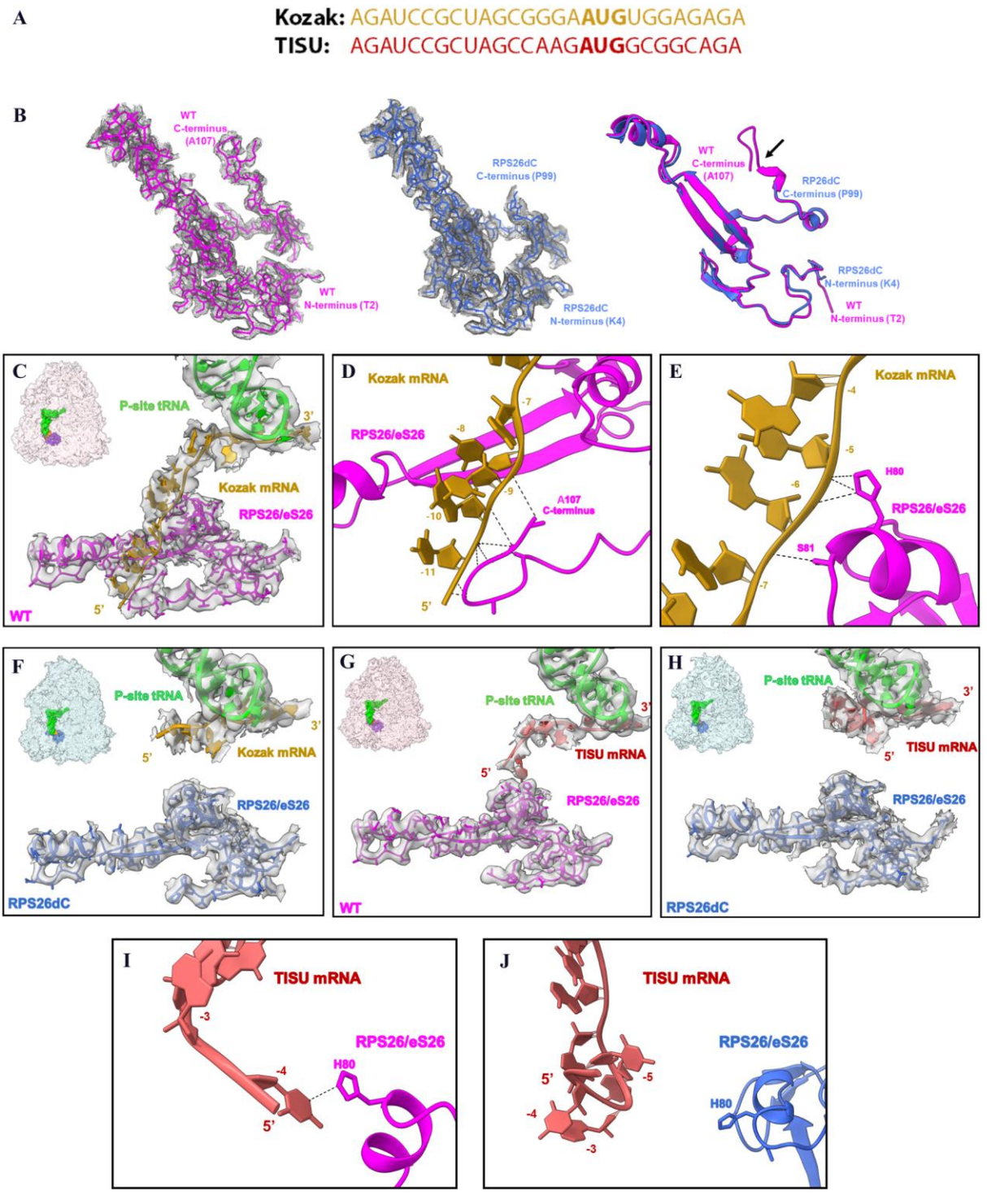
A
Kozak: AGAUCCGCUAGCGGGAAUGUGGAGAGA
TISU: AGAUCCGCUAGCCAAGAUGGCGGCAGA
B
WT C-terminus (A107)
WT N-terminus (T2)
RPS26dC C-terminus (P99)
RPS26dC N-terminus (K4)
WT C-terminus (A107)
RP26dC C-terminus (P99)
RPS26dC N-terminus (K4)
WT N-terminus (T2)
C
P-site tRNA
3'
Kozak mRNA
RPS26/eS26
5'
WT
D
Kozak mRNA
RPS26/eS26
-7
-8
-9
-10
-11
A107 C-terminus
5'
E
Kozak mRNA
-4
-5
-6
H80
RPS26/eS26
S81
-7
F
P-site tRNA
3'
5'
Kozak mRNA
RPS26/eS26
RPS26dC
G
P-site tRNA
3'
TISU mRNA
5'
RPS26/eS26
WT
H
P-site tRNA
3'
5'
TISU mRNA
RPS26/eS26
RPS26dC
I
TISU mRNA
-3
RPS26/eS26
-4
H80
5'
J
TISU mRNA
RPS26/eS26
5'
-5
-4
H80
-3

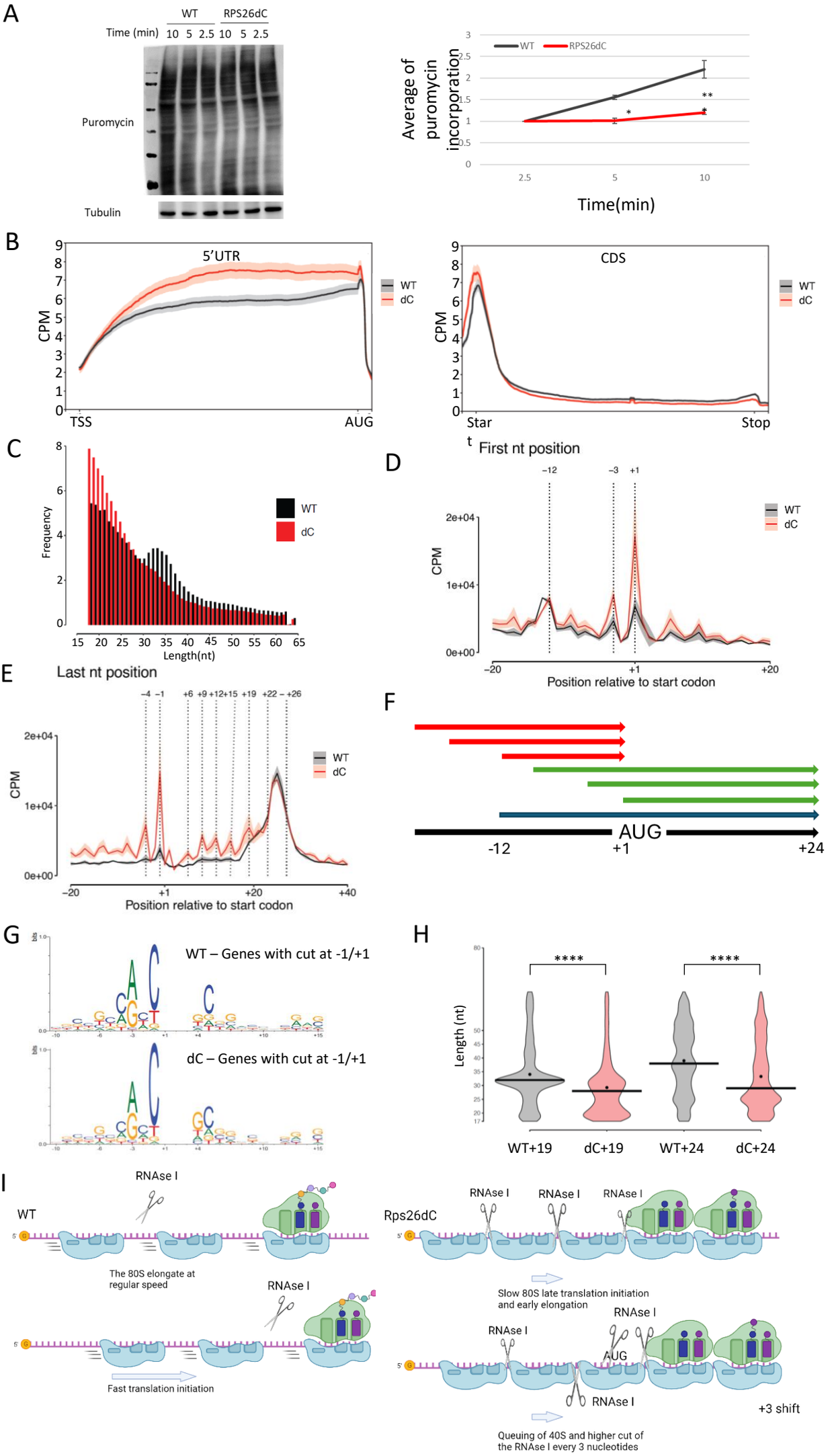
A
WT
RPS26dC
Time (min) 10 5 2.5 10 5 2.5
Puromycin
Tubulin
Average of puromycin incorporation
WT
RPS26dC
Time(min)
B
5'UTR
CDS
CPM
WT
dC
TSS
AUG
Star
Stop
C
Frequency
Length(nt)
D
First nt position
Position relative to start codon
E
Last nt position
Position relative to start codon
F
AUG
-12
+1
+24
G
WT – Genes with cut at -1/+1
dC – Genes with cut at -1/+1
H
Length (nt)
WT+19
dC+19
WT+24
dC+24
I
RNAse I
WT
The 80S elongate at regular speed
Fast translation initiation
Rps26dC
Slow 80S late translation initiation and early elongation
AUG
+3 shift
Queuing of 40S and higher cut of the RNAse I every 3 nucleotides

A

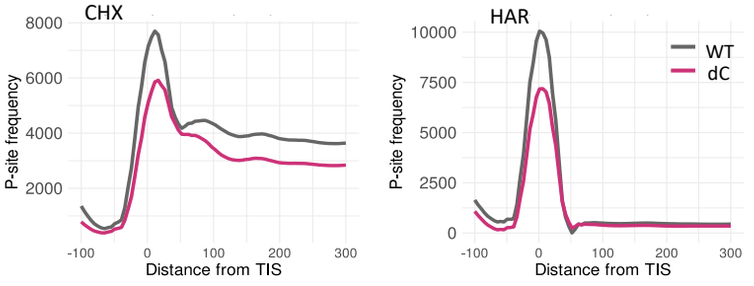

B

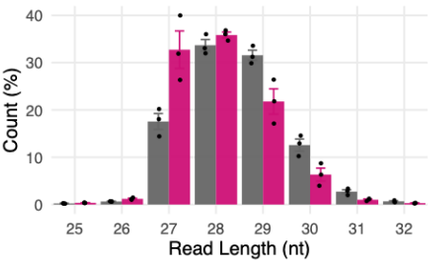

C

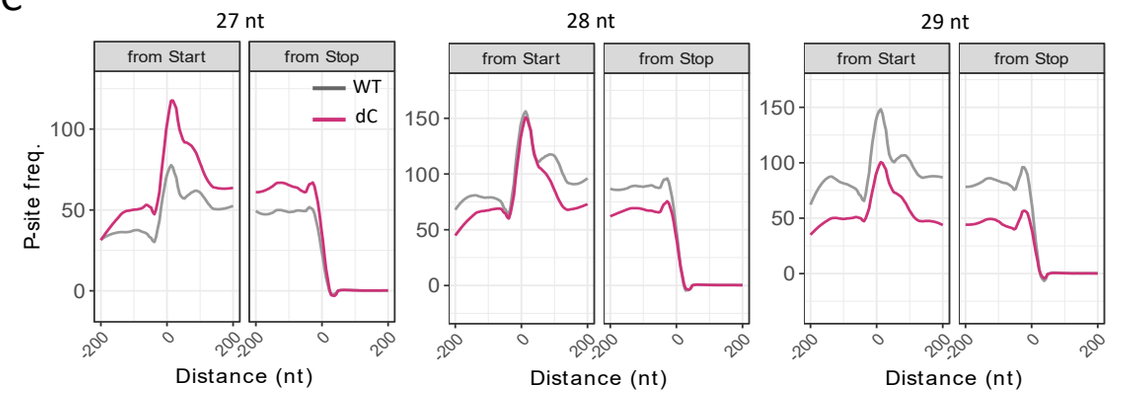

D

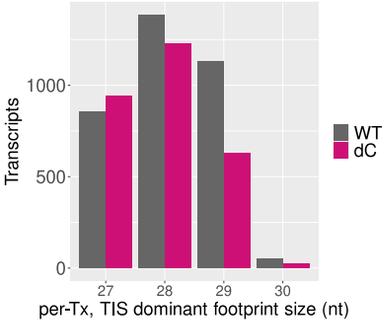

E

Differential Translation Efficiency

Regulation	Gene count
Down	309
Up	184

F

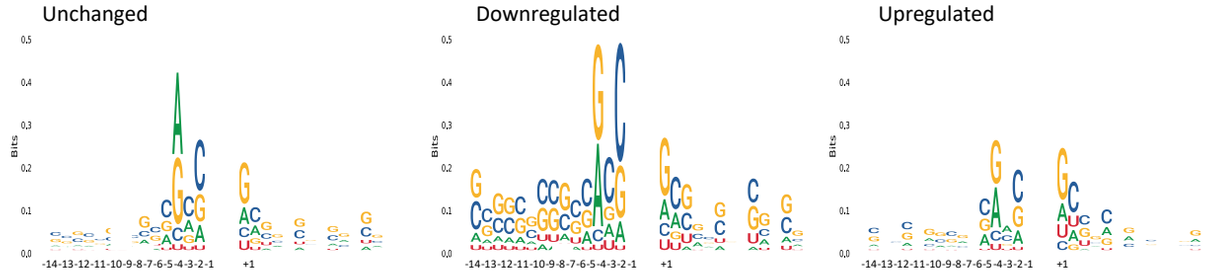

G

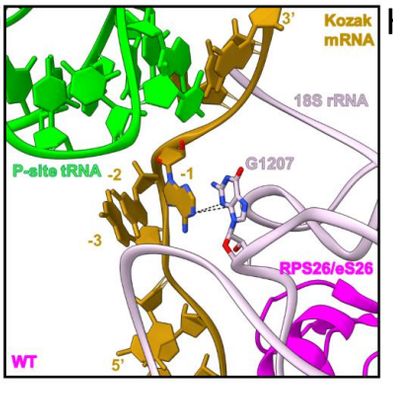

H

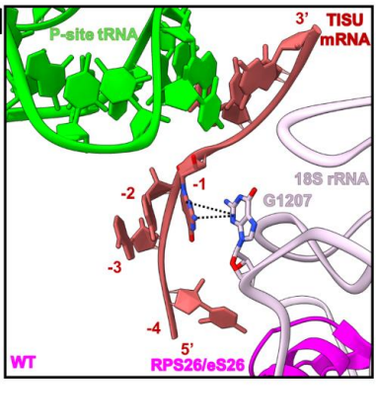

I

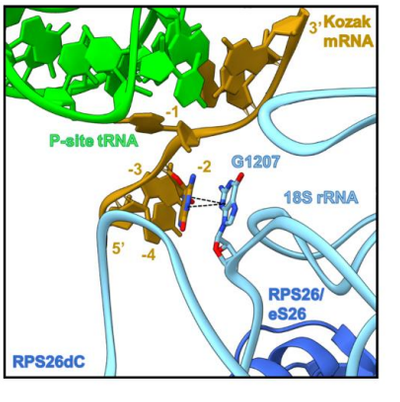

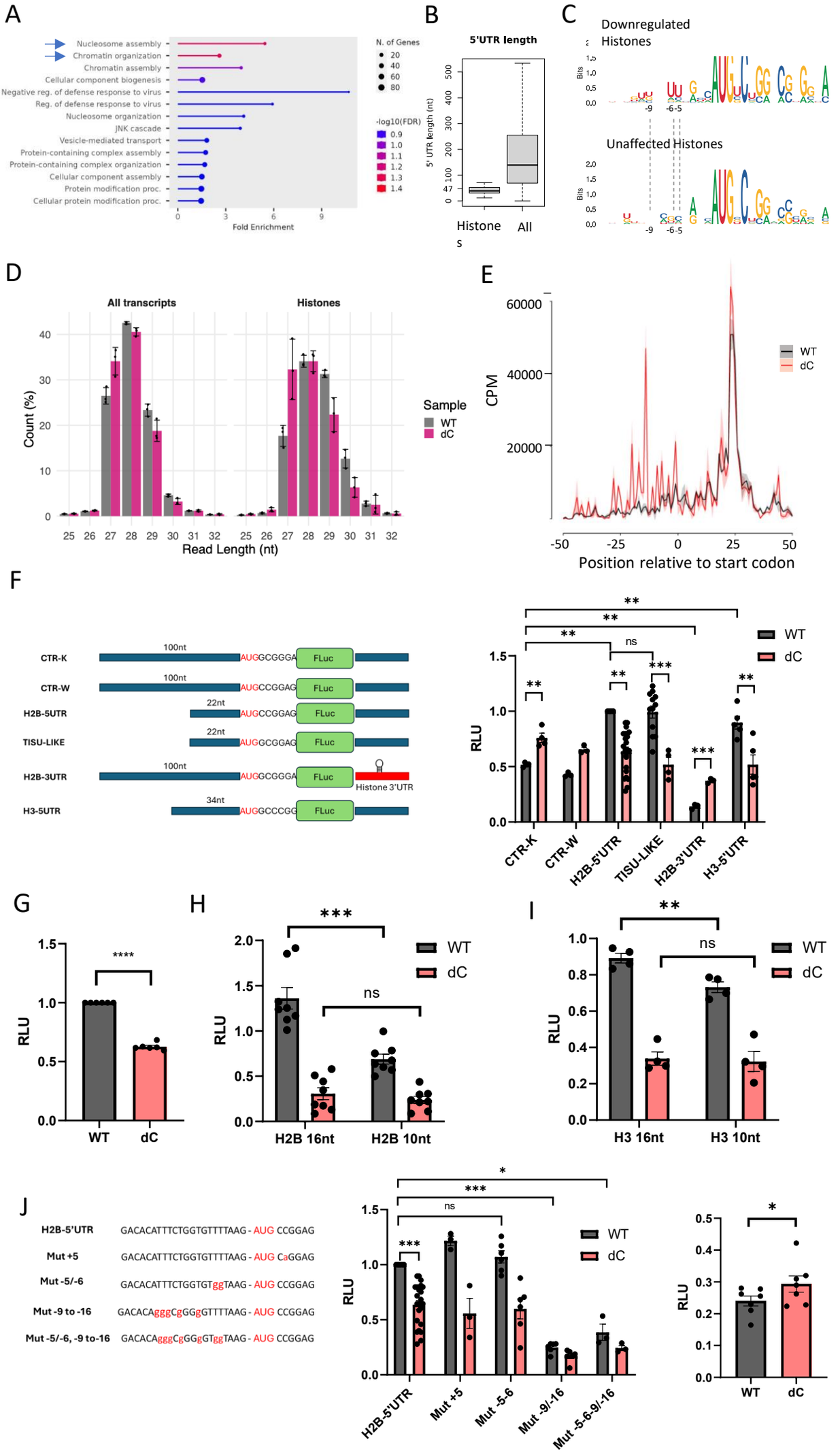
A
Nucleosome assembly
Chromatin organization
Chromatin assembly
Cellular component biogenesis
Negative reg. of defense response to virus
Reg. of defense response to virus
Nucleosome organization
JNK cascade
Vesicle-mediated transport
Protein-containing complex assembly
Protein-containing complex organization
Cellular component assembly
Protein modification proc.
Cellular protein modification proc.
Fold Enrichment
N. of Genes
-log10(FDR)
B
5'UTR length
5' UTR length (nt)
Histones
All
C
Downregulated Histones
Unaffected Histones
Bits
D
All transcripts
Histones
Count (%)
Read Length (nt)
Sample
WT
dC
E
CPM
Position relative to start codon
F
CTR-K
CTR-W
H2B-5UTR
TISU-LIKE
H2B-3UTR
H3-5UTR
100nt
22nt
34nt
AUGGCGGGA
AUGCCGGAG
AUGGCCCGG
FLuc
Histone 3'UTR
RLU
G
H
I
H2B 16nt
H2B 10nt
H3 16nt
H3 10nt
J
H2B-5'UTR GACACATTTCTGGTGTTTTAAG - AUG CCGGAG
Mut +5 GACACATTTCTGGTGTTTTAAG - AUG CaGGAG
Mut -5/-6 GACACATTTCTGGTGTggTAAG - AUG CCGGAG
Mut -9 to -16 GACACAgggCgGGgGTTTTAAG - AUG CCGGAG
Mut -5/-6, -9 to-16 GACACAgggCgGGgGTggTAAG - AUG CCGGAG
Mut +5
Mut -5-6
Mut -9/-16
Mut -5-6-9/-16

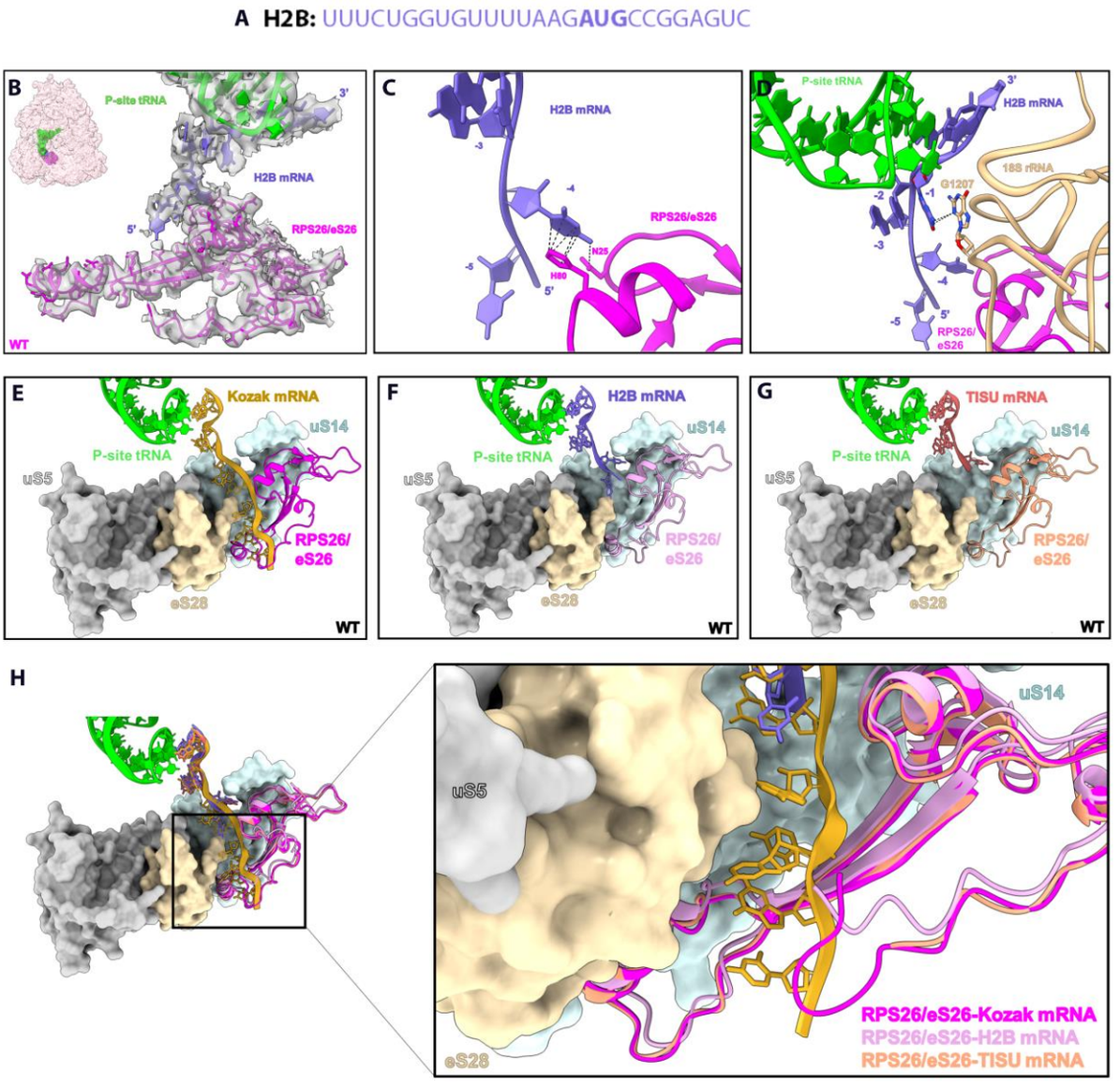
A H2B: UUUCUGGUGUUUUAAGAUGCCGGAGUC
B
P-site tRNA
3'
H2B mRNA
5'
RPS26/eS26
WT
C
H2B mRNA
-3
-4
RPS26/eS26
N25
H80
-5
5'
D
P-site tRNA
3'
H2B mRNA
18S rRNA
G1207
-2
-1
-3
-4
-5
5'
RPS26/
eS26
E
Kozak mRNA
uS14
P-site tRNA
uS5
RPS26/
eS26
eS28
WT
F
H2B mRNA
uS14
P-site tRNA
uS5
RPS26/
eS26
eS28
WT
G
TISU mRNA
uS14
P-site tRNA
uS5
RPS26/
eS26
eS28
WT
H
uS14
uS5
eS28
RPS26/eS26-Kozak mRNA
RPS26/eS26-H2B mRNA
RPS26/eS26-TISU mRNA

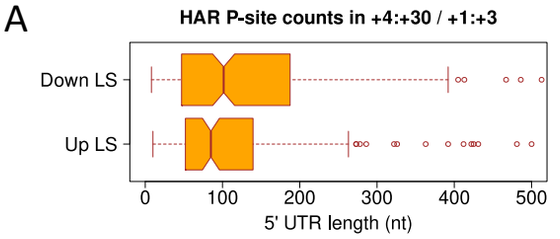
A
HAR P-site counts in +4:+30 / +1:+3
Down LS
Up LS
0
100
200
300
400
500
5' UTR length (nt)

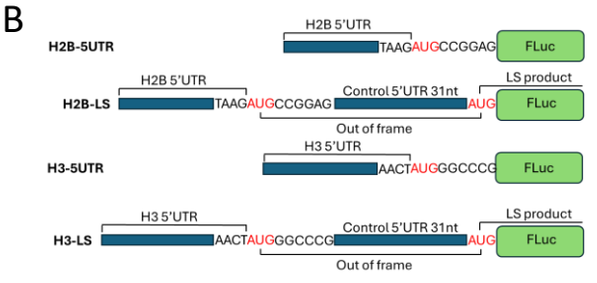
B
H2B-5UTR
H2B 5'UTR
TAAGAUGCCGGAG
FLuc
H2B-LS
Control 5'UTR 31nt
LS product
Out of frame
H3-5UTR
H3 5'UTR
AACTAUGGGCCCG
H3-LS

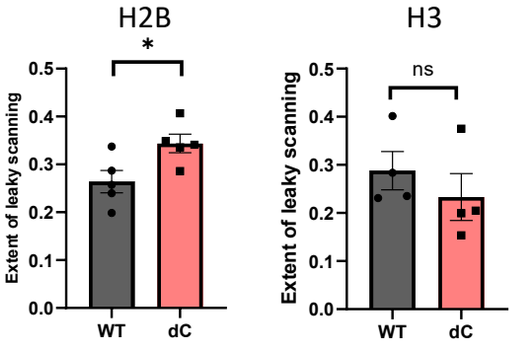
H2B
H3
*
ns
Extent of leaky scanning
WT
dC

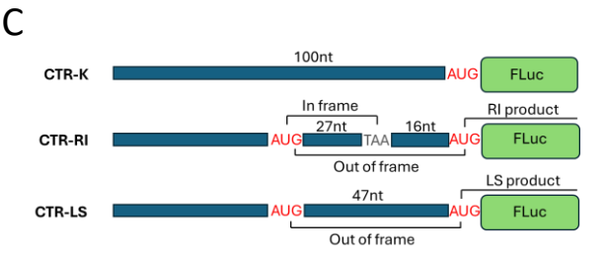
C
CTR-K
100nt
AUG
FLuc
CTR-RI
In frame
27nt
16nt
TAA
RI product
Out of frame
CTR-LS
47nt
LS product

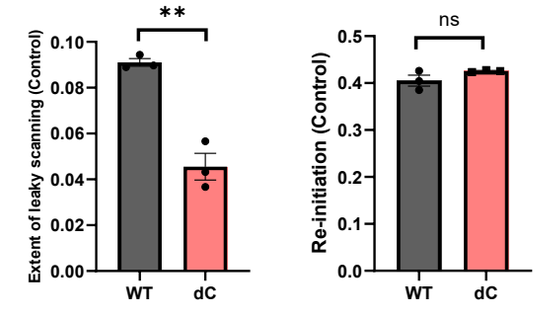
**
ns
Extent of leaky scanning (Control)
Re-initiation (Control)
WT
dC

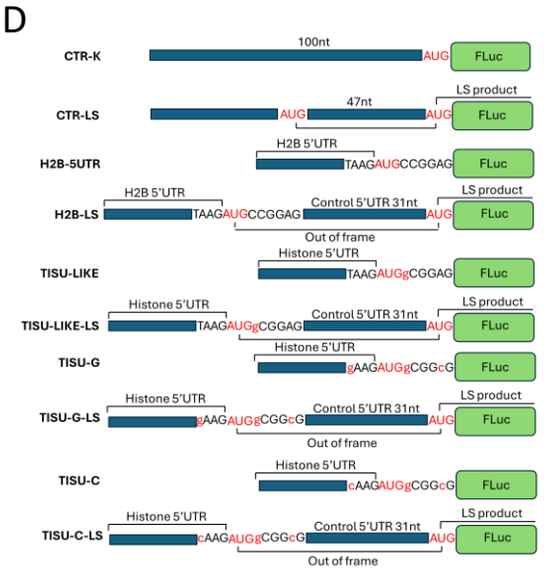
D
CTR-K
100nt
CTR-LS
47nt
H2B-5UTR
H2B-LS
TISU-LIKE
Histone 5'UTR
TISU-LIKE-LS
TISU-G
TISU-G-LS
TISU-C
TISU-C-LS
Control 5'UTR 31nt
LS product
Out of frame

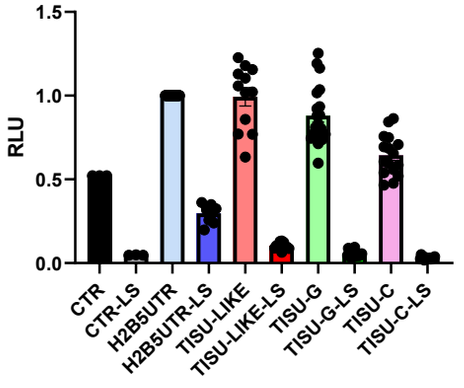
RLU
CTR
CTR-LS
H2B5UTR
H2B5UTR-LS
TISU-LIKE
TISU-LIKE-LS
TISU-G
TISU-G-LS
TISU-C
TISU-C-LS

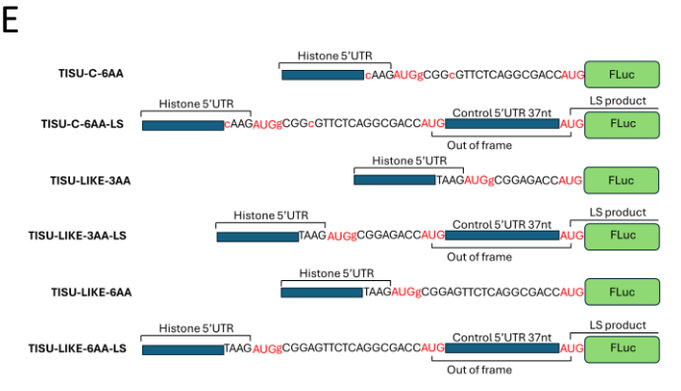
E
TISU-C-6AA
Histone 5'UTR
TISU-C-6AA-LS
Control 5'UTR 37nt
LS product
Out of frame
TISU-LIKE-3AA
TISU-LIKE-3AA-LS
TISU-LIKE-6AA
TISU-LIKE-6AA-LS

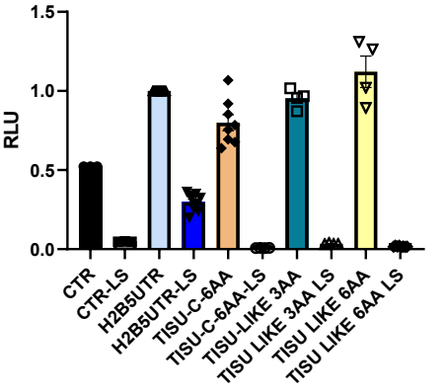
RLU
CTR
CTR-LS
H2B5UTR
H2B5UTR-LS
TISU-C-6AA
TISU-C-6AA-LS
TISU-LIKE 3AA
TISU-LIKE 3AA LS
TISU-LIKE 6AA
TISU-LIKE 6AA LS

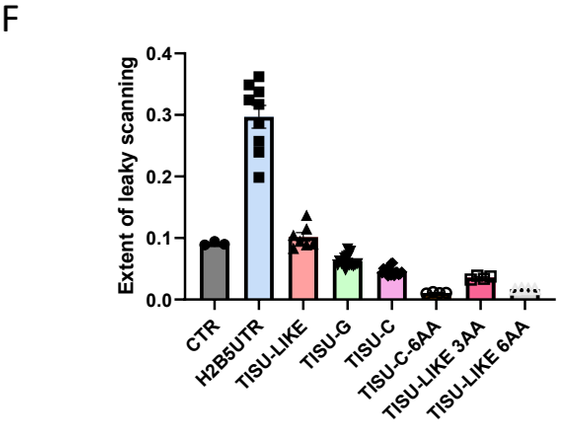
F
Extent of leaky scanning
CTR
H2B5UTR
TISU-LIKE
TISU-G
TISU-C
TISU-C-6AA
TISU-LIKE 3AA
TISU-LIKE 6AA